Comput Mech (2016) 58:957–979
DOI 10.1007/s00466-016-1326-7

ORIGINAL PAPER

Computation of the effective nonlinear mechanical response of lattice materials considering geometrical nonlinearities

Khaled ElNady[1] · **Ibrahim Goda**[1,2] · **Jean-François Ganghoffer**[1]

Received: 9 April 2016 / Accepted: 27 August 2016 / Published online: 15 September 2016

Abstract The asymptotic homogenization technique is presently developed in the framework of geometrical nonlinearities to derive the large strains effective elastic response of network materials viewed as repetitive beam networks. This works extends the small strains homogenization method developed with special emphasis on textile structures in Goda et al. (J Mech Phys Solids 61(12):2537–2565, 2013). A systematic methodology is established, allowing the prediction of the overall mechanical properties of these structures in the nonlinear regime, reflecting the influence of the geometrical and mechanical micro-parameters of the network structure on the overall response of the chosen equivalent continuum. Internal scale effects of the initially discrete structure are captured by the consideration of a micropolar effective continuum model. Applications to the large strain response of 3D hexagonal lattices and dry textiles exemplify the powerfulness of the proposed method. The effective mechanical responses obtained for different loadings are validated by FE simulations performed over a representative unit cell.

Keywords Geometrical nonlinearity · Micromechanical model · Discrete homogenization · Micropolar theory · Meso-scale unit-cell model · 2D and 3D textiles

---

✉ Ibrahim Goda
ibrahim.goda@univ-lorraine.fr

Khaled ElNady
khaled.el-nady@univ-lorraine.fr

Jean-François Ganghoffer
jean-francois.ganghoffer@univ-lorraine.fr

[1] LEMTA – Université de Lorraine, 2, Avenue de la Forêt de Haye, TSA 60604, 54054 Vandoeuvre, France

[2] Department of Industrial Engineering, Faculty of Engineering, Fayoum University, Fayoum 63514, Egypt

List of symbold

$\mathbf{B}_R$	Set of beams within the reference unit cell
$l^b = \varepsilon L^b$	Length of the beam b
$\mathbf{B}^{\mathrm{b}} = l^b \mathbf{e}_{\mathrm{x}}^{\mathrm{b}}$	Beam vector length
λ_{i}	Applied stretch in direction i
β^i	Curvilinear coordinates associated with the unit vectors
$\boldsymbol{\Gamma}$	Lagrangian wryness tensor
δ^{ib}	Shift factor for nodes belonging to a neighboring cell
$\mathbf{m}$	Couple stress tensor
$\mathbf{E}_{\mathrm{G}}$	Green–Lagrange strain
$\mathbf{R}$	Position vector of any material point within the effective continuum
$\varepsilon = l/L$	Small scale parameter
$\overline{\mathbf{R}}_{\mathrm{n}}$	Micropolar rotation tensor
$\mathbf{F}$	Deformation gradient
$\mathbf{S}^i$	Stress vectors
$\mathbf{F}_{\mathrm{e}}$	External force
$\boldsymbol{\sigma}$	Stress tensor
$\mathbf{F}^{\varepsilon\,\mathrm{b}}$	Resultant of forces at the nodes of a beam b
$\boldsymbol{\mu}^{\mathrm{i}}$	Couple stress vectors
$\boldsymbol{\varphi} = \varphi_i \mathbf{e}_i$	Microrotation vector
V	Total potential energy
$\boldsymbol{g}$	Jacobian of the transformation from Cartesian to curvilinear coordinates
$\mathbf{v}$	Virtual translational velocity field
$\mathbf{I}$	Second order identity tensor
$\mathrm{W}_{\mathrm{ext}}, \mathrm{W}_{\mathrm{int}}$	External and internal works
$\mathbf{K}_{\mathrm{T}}^{\mathrm{S}}$	Stress stifness matrix
$\mathbf{W}$	Virtual rotational velocity field
$\mathbf{K}_{\mathrm{T}}^{\mathrm{m}}$	Micropolar stiffness matrix
$\mathbb{Z}$	Set of cells of the macroscopic structure

1 Introduction

In recent years, different materials have been analyzed in the context of anisotropic finite-strain elasticity. These include composites, foam-like structures, textiles in the form of 2D and 3D preforms and synthetic solids. Cellular solids, by contrast to compact materials, are two or three dimensional bodies divided into cells, the walls of which are made of a solid material capable of undertaking large elastic deformations without plastic failure or fracture. There are numerous examples of such network structures, including repetitive large scale deployable structures like antenna, 3D textiles, cellular materials and especially auxetic structures having excellent damping and impact absorption capabilities [1].

The goal of this work is to compute the homogenized nonlinear response of network materials, based on an analysis performed over a repetitive unit cell at a mesoscopic level of the representative unit cell (abbreviated as RUC), intermediate between the microscopic level of the lattice and the macroscopic scale of the structure. We shall employ the discrete homogenization (DH in short) technique [2–5] which is perfectly suited to the discrete architecture of different types of networks, and which is extended to the nonlinear range in the present work. We shall consider that the observed nonlinear response is essentially due to the change of the network configuration (the orientation and length of the beams change with ongoing deformation).

Several models analyze simple topologies to obtain closed form expressions of the linear behavior of the lattice stiffness and strength, by solving the equilibrium problem of the unit cell [6–10]. These studies can offer insight into the general framework and theoretical basis for the development of a non linear constitutive model for lattice materials. Extensive reviews of these works can be found in [11,12].

The geometrical nonlinear behavior of cellular structures and network materials was extensively studied by [13,14], considering the example of foams, using simplified pin jointed model for which the bending contribution of the skeleton struts was neglected. Wang and Cuitino [15] proposed another approach where axial, bending and twisting deformations at local level were considered. One study based on homogenization technique was given in [16]. Linear effective models to analyze structures on the basis of a beam model were presented in [17,18], in which stretching and simultaneous bending occurs. More recently, Janus-Michalska [19] extended this linear model to construct the stress–strain relation and strain energy function for the hyperelastic cellular material with arbitrary symmetry. An alternative approach was proposed by Vigliotti et al. [20] using a computational homogenization to derive a nonlinear constitutive model for lattice materials.

A novel procedure for predicting the effective nonlinear elastic responses of repetitive lattices in the framework of the mechanics of micropolar continua through a combined linear and nonlinear discrete homogenization scheme shall be presented. The nonlinear stress–strain response will be computed incrementally for 2D and 3D structures subjected to different loading cases (uniaxial, biaxial, simple shear, and bending), taking into consideration changes of the structure geometry. The combination of the proposed incremental scheme with the homogenization method shall deliver both the classical and nonclassical properties.

The outline of this contribution is as follows: Sect. 2 is devoted to the description of the discrete homogenization method at both microscopic and mesoscopic scales. The homogenization technique and the expression of forces and moments in the framework of 3D Euler–Bernoulli beams are exposed. The algorithm used for the incremental procedure performing the update of variables at the lattice level accounting for the evolution of the lattice geometry will be described in Sect. 2. Numerical examples are proposed to illustrate the proposed methodology in Sect. 3, starting from the 3D hexagonal lattice and extending then the applications to the computation of the nonlinear response of 2D and 3D textile structures. In Sect. 4, the computed stress–strain homogenized responses are validated thanks to FE simulations performed over a representative unit cell. We conclude by a summary of the work and perspectives of developments are mentioned in Sect. 5.

A few words regarding notations are in order. Vectors and higher order tensors are denoted with boldface symbols. The summation convention on repeated indices is presently adopted, otherwise explicitly stated. The second order identity tensor is denoted **I**.

2 Microscopic and mesoscopic homogenization problems

The discrete homogenization method is a mathematical technique to derive the equivalent continuous medium behaviour of repetitive discrete structures; it is inspired from the homogenization of periodic media developed thirties years ago by [21,22] and more recently applied in [23,24]. It has been also combined with the energy method by [25] and applied to discrete homogenization. The interest of the discrete homogenization method is that it delivers the full compliance (or rigidity) matrix, reflecting the sometimes complex anisotropy of the so-built equivalent continuum; it is worthwhile noting that the material symmetry group of the discrete lattice is included in the material symmetry group of the homogenized medium [26]. Such complex constitutive laws may then nurture macroscopic simulations at the component level [27].

In the present approach, we rely on the so-called discrete homogenization method suitable for lattice materials comprising a periodic array of beams; instead of making full structural computations over the entire lattice—which would be computationally too expensive—we derive a nonlinear constitutive model at the intermediate mesoscopic scale based on a continuum description, avoiding the explicit description of the individual struts of the initial lattice. The DH method is first exposed in the linear small strains regime in order to compute the initial effective moduli of the effective substitution continuum; it is then extended to the nonlinear regime in order to account for the variation of the lattice geometry under an imposed kinematic loading over an identified representative unit cell. The nonlinear response of the lattice is homogenized at the RUC level, thereby providing both the stress–strain and couple stress–curvature relations, based on an incremental scheme accounting essentially for geometrical nonlinearities.

The nonlinear computations include as a first step the evaluation of the elastic properties in the small strains regime, followed by a succession of updating steps at the micro level (the microstructure of the unit cell geometry is updated), which entails an update of the homogenized mechanical fields at the mesoscopic level of the effective continuum.

2.1 Small strains homogenization: determination of the initial elastic response

The asymptotic expansion of the nodal displacement $\mathbf{u}^{\varepsilon}$ is written up to the second order as

$$\mathbf{u}^{\varepsilon}(\beta^{\varepsilon}) = \mathbf{u}_0(\beta^{\varepsilon}) + \varepsilon\mathbf{u}_1(\beta^{\varepsilon}) + \varepsilon^2\mathbf{u}_2(\beta^{\varepsilon}) \tag{1}$$

in which ε is the ratio of unit cell size to a characteristic dimension of the entire structure.

The displacement difference $\Delta\mathbf{U}^{\mathrm{b}\varepsilon}$ between the extremity and origin node of each beam is expressed by a Taylor series development, according to

$$\begin{aligned}\Delta\mathbf{U}^{\mathrm{b}\varepsilon} &= \mathbf{u}^{\varepsilon}(E(b)) - \mathbf{u}^{\varepsilon}(O(b)) \\ &= \underbrace{\varepsilon\left(\mathbf{u}_1^{E_{R(b)}}(\beta^{\varepsilon}) - \mathbf{u}_1^{O_{R(b)}}(\beta^{\varepsilon}) + \frac{\partial\mathbf{u}_0(\beta^{\varepsilon})}{\partial\beta^i}\delta^{ib}\right)}_{\Delta\mathrm{U}_1^{\mathrm{b}}} \\ &\quad + \varepsilon^2\underbrace{\left(\mathbf{u}_2^{E_{R(b)}}(\beta^{\varepsilon}) - \mathbf{u}_2^{O_{R(b)}}(\beta^{\varepsilon})\right)}_{\Delta\mathrm{U}_2^{\mathrm{b}}} \\ &= \varepsilon\Delta\mathbf{U}_1^{\mathrm{b}} + \varepsilon^2\Delta\mathbf{U}_2^{\mathrm{b}}\end{aligned} \tag{2}$$

with δ^{ib} the shift factor (equal to ±1) for nodes belonging to a neighbouring cell, and nil for nodes located inside the considered cell.

The asymptotic expansion of the nodal microrotation $\boldsymbol{\varphi}^{n\varepsilon}$ is here limited to the first order in ε; it is defined successively at the origin and extremity of each beam as

$$\begin{aligned}\boldsymbol{\varphi}^{O(b)\varepsilon} &= \boldsymbol{\varphi}_0^{O_{R(b)}} + \varepsilon\boldsymbol{\varphi}_1^{O_{R(b)}};\ \boldsymbol{\varphi}^{E(b)\varepsilon} = \boldsymbol{\varphi}_0^{E_{R(b)}} \\ &\quad + \varepsilon\left(\frac{\partial\boldsymbol{\varphi}_0}{\partial\beta^i}\delta^{ib} + \boldsymbol{\varphi}_1^{E_{R(b)}}\right)\end{aligned} \tag{3}$$

wherein we have parameterized any point within the surface element representative of the lattice by curvilinear coordinates β^i; this allows treating lattices with curved material lines following the fibers in their reference state.

Note that the present beam model and subsequent derivations of the effective mechanical response are not specific to textile materials, but can be applied to any lattice materials showing interactions between tension, bending and torsion.

The equilibrium of forces (self-equilibrium in the absence of external forces) writes in virtual power form for the whole lattice and after asymptotic development as

$$\sum_{\upsilon^{\mathrm{i}}\in\mathbb{Z}^3}\sum_{\mathrm{b}\in\mathbf{B}_{\mathrm{R}}}\mathbf{F}^{\varepsilon\,\mathrm{b}}\cdot\left(\mathbf{v}^{\varepsilon}(\mathrm{O}(\mathrm{b})) - \mathbf{v}^{\varepsilon}(\mathrm{E}(\mathrm{b}))\right) = 0 \tag{4}$$

with $\mathbf{v}(\cdot)$ a virtual velocity field vanishing on the unit cell edges. The force vector $\mathbf{F}^{\varepsilon\,\mathrm{b}}$decomposes into a normal and transverse forces as

$$\mathbf{F}^{\varepsilon\,\mathrm{b}} = \mathrm{F}_{\mathrm{x}}^{\varepsilon\,\mathrm{b}}\mathbf{e}_{\mathrm{x}} + \mathrm{F}_{\mathrm{y}}^{\varepsilon\,\mathrm{b}}\mathbf{e}_{\mathrm{y}} + \mathrm{F}_{\mathrm{z}}^{\varepsilon\,\mathrm{b}}\mathbf{e}_{\mathrm{z}} \tag{5}$$

We denote by $\mathbf{B}_R$, in Eq. (4) the set of beams within the reference unit cell. The normal and transverse forces exerted on the beam extremities are obtained after lengthy calculations in the framework of 3D Euler–Bernoulli beams, expressed in Appendix 1.

In (5), the unit vectors $\mathbf{e}_x = \left[Cxx'\ Cyx'\ Czx'\right]^T$,$\mathbf{e}_y = \left[Cxy'\ Cyy'\ Czy'\right]^T$, and $\mathbf{e}_z = \left[Cxz'\ Cyz'\ Czz'\right]^T$, where $Cxx' = \cos\ \theta_x$,$Cyx' = \cos\ \theta_y$, and $Czx' = \cos\ \theta_z$ are the direction cosines of x', describing the transformation between the local and global coordinate system in 3D (Fig. 1). Similarly, the components of $\mathbf{e}_y$ and $\mathbf{e}_z$ are the direction cosines of y' and z', respectively.

In a second step, we write the discrete equilibrium of moments, which can be expressed in two different ways: one first considers the equilibrium of moments for the unit cell nodes, which is necessary to solve for the kinematic unknowns; it writes in asymptotic form as

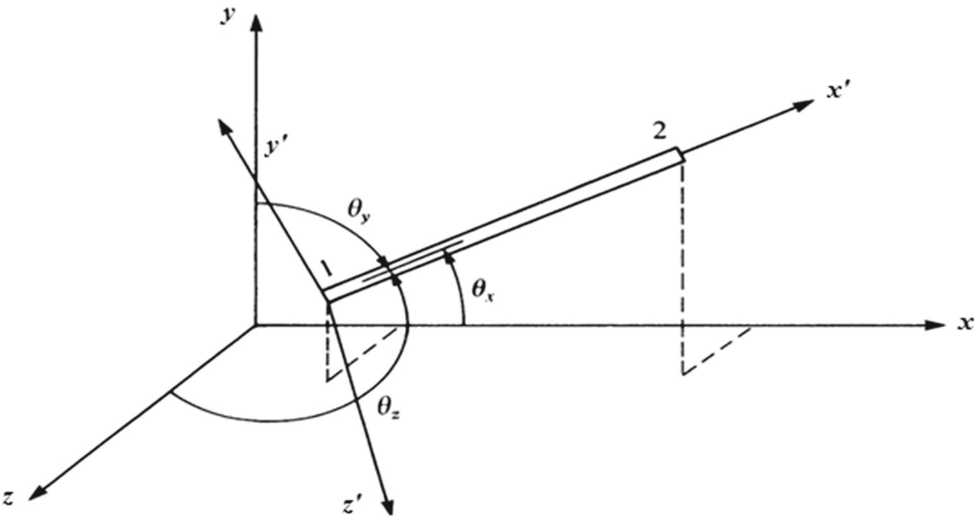

Fig. 1 Direction cosines associated with the x axis

$$\sum_{\upsilon^i\in\mathbb{Z}^3}\sum_{b\in\mathbf{B}_R}\left(\mathbf{M}^{O(b)\varepsilon}\cdot\mathbf{w}^{\varepsilon}\left(O(b)\right)+\mathbf{M}^{E(b)\varepsilon}\cdot\mathbf{w}^{\varepsilon}\left(E(b)\right)\right)=0 \tag{6}$$

Another writing involving the local equilibrium of each individual beam is considered for the purpose of homogenization; equilibrium is here written at the center of each beam in asymptotic form as

$$\sum_{\upsilon^i\in\mathbb{Z}^3}\sum_{b\in\mathbf{B}_R}\Big(\mathbf{M}^{O(b)\varepsilon}\cdot\mathbf{w}^{\varepsilon}\left(O(b)\right)+\mathbf{M}^{E(b)\varepsilon}\cdot\mathbf{w}^{\varepsilon}\left(E(b)\right)$$
$$+\varepsilon l^b\left(\mathbf{e}_x\wedge\mathbf{F}^{\varepsilon b}\right).\mathbf{w}^{\varepsilon}\left(C(b)\right)\Big)=0 \tag{7}$$

with $\mathbf{w}(\cdot)$ the virtual rotational velocity field and $\mathbf{M}^{O(b)}$, $\mathbf{M}^{E(b)}$ the moments exerted on the beam extremities, expressed in Appendix 1. Details related to the first order homogenization in the micropolar framework can be found in [1,28,29]. In the forthcoming development, a circular section of the beams is considered, hence the following geometrical parameters are computed: the cross-sectional area $A^{\varepsilon b}=\pi(\varepsilon r^b)^2$, the quadratic moment of the beam $I_y^{\varepsilon b}=I_z^{\varepsilon b}=\pi\frac{(\varepsilon r^b)^4}{4}$, and the torsional constant $J^{\varepsilon b}=\pi\frac{\left(\varepsilon r^b\right)^4}{2}$.

The homogenization of the discrete equilibrium of forces, Eq. (4), leads to the following continuum self-equilibrium in virtual power form

$$\int_{\Omega}\mathbf{S}^i\cdot\frac{\partial\mathbf{v}(\beta)}{\partial\beta^{\mathrm{i}}}d\beta=0 \tag{8}$$

with the stress vector $\mathbf{S}^i$ therein splitting into first and second order contributions, viz. $\mathbf{S}^i=\mathbf{S}_1^i+\varepsilon\mathbf{S}_2^i$, with

$$\mathbf{S}_1^i=\sum_{b\in\mathbf{B}_R}\begin{pmatrix}\frac{\pi E_s^b\left(r^b\right)^2}{l^b}\left(\mathbf{e}_x\cdot\Delta\mathbf{U}_1^{\mathrm{b}}\right)\mathbf{e}_x\\+\left(\frac{3\pi E_s^b\left(r^b\right)^4}{\left(l^b\right)^3}\left(\mathbf{e}_y\cdot\Delta\mathbf{U}_1^{\mathrm{b}}-\frac{l^b}{2}\left(\mathbf{e}_z\cdot\left(\boldsymbol{\varphi}_0^{O_{R(b)}}+\boldsymbol{\varphi}_0^{E_{R(b)}}\right)\right)\right)\right)\mathbf{e}_y\\+\left(\frac{3\pi E_s^b\left(r^b\right)^4}{\left(l^b\right)^3}\left(\mathbf{e}_z\cdot\Delta\mathbf{U}_1^{\mathrm{b}}+\frac{l^b}{2}\left(\mathbf{e}_y\cdot\left(\boldsymbol{\varphi}_0^{O_{R(b)}}+\boldsymbol{\varphi}_0^{E_{R(b)}}\right)\right)\right)\right)\mathbf{e}_z\end{pmatrix}\delta^{ib}$$

$$\mathbf{S}_2^i=\sum_{b\in\mathbf{B}_R}\begin{pmatrix}\frac{\pi E_s^b\left(r^b\right)^2}{l^b}\left(\mathbf{e}_x\cdot\Delta\mathbf{U}_2^{\mathrm{b}}\right)\mathbf{e}_x\\+\left(\frac{3\pi E_s^b\left(r^b\right)^4}{\left(L^b\right)^3}\left(\mathbf{e}_y\cdot\Delta\mathbf{U}_2^{\mathrm{b}}\right.\right.\\\left.\left.-\frac{l^b}{2}\left(\mathbf{e}_z\left(\boldsymbol{\varphi}_1^{O_{R(b)}}+\boldsymbol{\varphi}_1^{E_{R(b)}}+\frac{\partial\boldsymbol{\varphi}_0}{\partial\beta^i}\delta^{ib}\right)\right)\right)\right)\mathbf{e}_y\\+\left(\frac{3\pi E_s^b\left(r^b\right)^4}{\left(l^b\right)^3}\left(\mathbf{e}_z\cdot\Delta\mathbf{U}_2^{\mathrm{b}}\right.\right.\\\left.\left.+\frac{l^b}{2}\left(\mathbf{e}_y\cdot\left(\boldsymbol{\varphi}_1^{O_{R(b)}}+\boldsymbol{\varphi}_1^{E_{R(b)}}+\frac{\partial\boldsymbol{\varphi}_0}{\partial\beta^i}\delta^{ib}\right)\right)\right)\right)\mathbf{e}_z\end{pmatrix}\delta^{ib} \tag{9}$$

Similarly to the previous development, the moment equilibrium (7) is homogenized after inserting the asymptotic expansion of the virtual rotation rate, expression (36) in Appendix 1: passing to the limit ε → 0 in the discrete sum, this leads to the following continuous self-equilibrium in virtual power form

$$\int_{\Omega}\boldsymbol{\mu}^i\cdot\frac{\partial\mathbf{w}(\beta)}{\partial\beta^{\mathrm{i}}}d\beta=0 \tag{10}$$

with the couple stress vector $\boldsymbol{\mu}^i$ which incorporates the moments, identified on two orders, viz. $\boldsymbol{\mu}^i=\varepsilon\boldsymbol{\mu}_1^i+\varepsilon^2\boldsymbol{\mu}_2^i$, with the first and second order contributions given by

$$\boldsymbol{\mu}_1^{\mathrm{i}}=\sum_{\mathrm{b}\in\mathbf{B}_R}\left(\frac{1}{2}\left(\mathrm{M}_{1\mathrm{y}}^{\mathrm{E(b)}}-\mathrm{M}_{1\mathrm{y}}^{\mathrm{O(b)}}\right)\mathbf{e}_{\mathrm{y}}+\frac{1}{2}\left(\mathrm{M}_{1\mathrm{z}}^{\mathrm{E(b)}}-\mathrm{M}_{1\mathrm{z}}^{\mathrm{O(b)}}\right)\mathbf{e}_{\mathrm{z}}\right)\delta^{\mathrm{ib}},$$

$$\boldsymbol{\mu}_2^i=\sum_{\mathrm{b}\in\mathbf{B}_R}\Big(\mathrm{M}_{2\mathrm{x}}^{\mathrm{E(b)}}\mathbf{e}_{\mathrm{x}}+\frac{1}{2}\left(\mathrm{M}_{2\mathrm{y}}^{\mathrm{E(b)}}-\mathrm{M}_{2\mathrm{y}}^{\mathrm{O(b)}}\right)\mathbf{e}_{\mathrm{y}}$$
$$+\frac{1}{2}\left(\mathrm{M}_{2\mathrm{z}}^{\mathrm{E(b)}}-\mathrm{M}_{2\mathrm{z}}^{\mathrm{O(b)}}\right)\mathbf{e}_{\mathrm{z}}\Big)\delta^{\mathrm{ib}} \tag{11}$$

The subscripts 1 and 2 in these expressions refer respectively to the first and second order moments in expressions (32)–(34) in Appendix 1.

The general form of the constitutive equations can presently be identified from the expressions of the homogenized stress and couple stress tensors together with $\mathbf{S}^{\mathrm{i}}$ and $\boldsymbol{\mu}^{\mathrm{i}}$ expressions as:

$$\begin{aligned}\boldsymbol{\sigma} &= \frac{1}{g}\mathbf{S}^{\mathrm{i}} \otimes \frac{\partial \mathbf{R}}{\partial \beta^{\mathrm{i}}} = \frac{1}{g}\left(\mathbf{S}_1^{\mathrm{i}} + \varepsilon \mathbf{S}_2^{\mathrm{i}}\right) \otimes \frac{\partial \mathbf{R}}{\partial \beta^{\mathrm{i}}} \\ &= \underbrace{\frac{1}{g}\mathbf{S}_1^{\mathrm{i}} \otimes \frac{\partial \mathbf{R}}{\partial \beta^{\mathrm{i}}}}_{[\mathbf{K}^s]\{\boldsymbol{\varepsilon}\}} + \underbrace{\frac{1}{g}\varepsilon \mathbf{S}_2^{\mathrm{i}} \otimes \frac{\partial \mathbf{R}}{\partial \beta^{\mathrm{i}}}}_{[\mathbf{H}]\{\boldsymbol{\chi}\}} \\ \mathbf{m} &= \frac{1}{g}\boldsymbol{\mu}^{\mathrm{i}} \otimes \frac{\partial \mathbf{R}}{\partial \beta^{\mathrm{i}}} = \frac{1}{g}\left(\varepsilon \boldsymbol{\mu}_1^{\mathrm{i}} + \varepsilon^2 \boldsymbol{\mu}_2^{\mathrm{i}}\right) \otimes \frac{\partial \mathbf{R}}{\partial \beta^{\mathrm{i}}} \\ &= \underbrace{\frac{1}{g}\varepsilon \boldsymbol{\mu}_1^{\mathrm{i}} \otimes \frac{\partial \mathbf{R}}{\partial \beta^{\mathrm{i}}}}_{[\mathbf{H}]\{\boldsymbol{\varepsilon}\}} + \underbrace{\frac{1}{g}\varepsilon^2 \boldsymbol{\mu}_2^{\mathrm{i}} \otimes \frac{\partial \mathbf{R}}{\partial \beta^{\mathrm{i}}}}_{[\mathbf{K}^{\mu}]\{\boldsymbol{\chi}\}} \end{aligned} \tag{12}$$

with $\boldsymbol{g}$ the Jacobian of the transformation from Cartesian to curvilinear coordinates and $\mathbf{R}$ the position vector of any material point within the effective continuum.

Since for all periodical uniform structures endowed with a central symmetry, the stiffness coefficients are invariant under a coordinate inversion, this entails that the pseudo-tensor $\mathbf{H}_{ijkl}$ vanishes [26]. The previous constitutive equations then implies that the vectors $\boldsymbol{\mu}_1^{\mathrm{i}}$ and $\mathbf{S}_2^{i}$ in (12) vanish; this leads to an important simplification of the stress and couple stress vectors respectively,

$$\begin{aligned}\mathbf{S}^{i} &= \mathbf{S}_1^{i} = \sum_{b \in \mathbf{B}_R} \left(F_{x1}^{b}\mathbf{e}_x + F_{y1}^{b}\mathbf{e}_y + F_{z1}^{b}\mathbf{e}_z\right)\delta^{ib} \text{ and} \\ \boldsymbol{\mu}^{\mathrm{i}} &= \boldsymbol{\mu}_2^{\mathrm{i}} = \sum_{b \in \mathbf{B}_R} \left(M_{2x}^{E(b)}\mathbf{e}_x + \frac{1}{2}\left(M_{2y}^{E(b)} - M_{2y}^{O(b)}\right)\mathbf{e}_y \right. \\ &\quad \left. + \frac{1}{2}\left(M_{2z}^{E(b)} - M_{2z}^{O(b)}\right)\mathbf{e}_z\right)\delta^{ib}\end{aligned}$$

with F_{x1}^{b}, F_{y1}^{b}, F_{z1}^{b}, M_{2x}^{n}, M_{2y}^{n}, and M_{2z}^{n} respectively, the first order normal and transverse forces and the second order moment about x', y', and z'. Those expressions still involve the unknown displacements $\mathbf{u}_1^{n}$, $\mathbf{u}_2^{n}$ and rotations $\boldsymbol{\varphi}_0^{n}$, $\boldsymbol{\varphi}_1^{n}$, which are determined for all nodes by solving the equilibrium equations (4) and (6).

2.2 Large configuration changes of lattices by the DH method

We next expose the extension of the previous DH method to the nonlinear regime, in order to account for the large changes of configuration of the networks. This shall lead to an algorithm for the computation of the large strains response of the considered networks. The analysis is performed over the RUC selected as the lattice unit cell, relying on recent results [20] showing that the RUC size has no effect on the predicted homogenized response in the nonlinear regime, as long as no bifurcations occur.

2.2.1 Microscopic incremental problem over the lattice

In this subsection, we extend the linear framework so far adopted and consider the impact of a variation of the lattice geometry on the effective structure behaviour. We accordingly write down the non-linear equilibrium problem associated to the large perturbations of the network; the nonlinearity is due to the beam directors and beam lengths changing with the applied loading.

As a starting point, the incremental form of the principle of virtual displacements in continuum mechanics is expressed

$$\delta\,\mathrm{W}_{\mathrm{ext}} - \delta\,\mathrm{W}_{\mathrm{int}} = 0 \Rightarrow \delta\,\mathrm{V} = \int_{\mathrm{D}} \boldsymbol{\sigma} \cdot \delta\,\mathbf{E}_{\mathrm{G}}\mathrm{dV} = \mathbf{F}_{\mathrm{e}} \cdot \delta\,\mathbf{u} \tag{13}$$

with $\delta\mathrm{W}_{\mathrm{ext}}$, $\delta\mathrm{W}_{\mathrm{int}}$, V, $\mathbf{E}_{\mathrm{G}}$, $\mathbf{F}_{\mathrm{e}}$ the virtual variation of the external and internal works, the total potential energy, the Green–Lagrange strain and the external force respectively.

We write down the non-linear equilibrium problem associated to the large perturbations of the network; the nonlinearity is due to the large displacements and microrotations, which in turn are responsible for the large changes of beam directors orientation and beam lengths. From this, one can set up a kinematically driven scheme, based on the incremental writing of the equilibrium equations in translation and rotation (we refer the reader to the small strain equations (4) and (7) respectively), successively the two following equations

$$\begin{aligned}&\forall \mathbf{v} \in R^3, \quad \sum_{\mathrm{b} \in \mathbf{B}_R} \left(\delta\,\mathrm{F}_{\mathrm{x}}^{\varepsilon\,\mathrm{b(k)}}\mathbf{e}_{\mathrm{x}}^{\mathrm{b(k)}} + \mathrm{F}_{\mathrm{x}}^{\varepsilon\,\mathrm{b(k)}}\delta\mathbf{e}_{\mathrm{x}}^{\mathrm{b(k)}}\right) \\ &\quad \cdot \Delta\mathbf{v} + \sum_{\mathrm{b} \in \mathbf{B}_R} \left(\mathrm{F}_{\mathrm{x}}^{\varepsilon\,\mathrm{b(k)}}\mathbf{e}_{\mathrm{x}}^{\mathrm{b(k)}}\right) \cdot \Delta\mathbf{v} \\ &\quad + \sum_{\mathrm{b} \in \mathbf{B}_R} \left(\delta\mathrm{F}_{\mathrm{y}}^{\varepsilon\,\mathrm{b(k)}}\mathbf{e}_{\mathrm{y}}^{\mathrm{b(k)}} + \mathrm{F}_{\mathrm{y}}^{\varepsilon\,\mathrm{b(k)}}\delta\mathbf{e}_{\mathrm{y}}^{\mathrm{b(k)}}\right) \cdot \Delta\mathbf{v} \\ &\quad + \sum_{\mathrm{b} \in \mathbf{B}_R} \left(\mathrm{F}_{\mathrm{y}}^{\varepsilon\,\mathrm{b(k)}}\mathbf{e}_{\mathrm{y}}^{\mathrm{b(k)}}\right) \cdot \Delta\mathbf{v} \\ &\quad + \sum_{\mathrm{b} \in \mathbf{B}_R} \left(\delta\,\mathrm{F}_{\mathrm{z}}^{\varepsilon\,\mathrm{b(k)}}\mathbf{e}_{\mathrm{z}}^{\mathrm{b(k)}} + \mathrm{F}_{\mathrm{z}}^{\varepsilon\,\mathrm{b(k)}}\,\delta\,\mathbf{e}_{\mathrm{z}}^{\mathrm{b(k)}}\right) \cdot \Delta\mathbf{v} \\ &\quad + \sum_{\mathrm{b} \in \mathbf{B}_R} \left(\mathrm{F}_{\mathrm{z}}^{\varepsilon\,\mathrm{b(k)}}\mathbf{e}_{\mathrm{z}}^{\mathrm{b(k)}}\right) \cdot \Delta\mathbf{v} = 0, \quad \forall \mathbf{w} \in R^3, \\ &\quad \sum_{\mathrm{b} \in \mathbf{B}_R} \left(\delta\left(\mathrm{M}_{\mathrm{x}}^{\varepsilon\,\mathrm{E(b)(k)}}\mathbf{e}_{\mathrm{x}}^{\mathrm{b(k)}} + \mathrm{M}_{\mathrm{y}}^{\varepsilon\,\mathrm{E(b)(k)}}\mathbf{e}_{\mathrm{y}}^{\mathrm{b(k)}}\right.\right.\end{aligned}$$

Fig. 2 Variation of beam orientation (*left*) and length (*right*)

$$
\begin{aligned}
&+ \mathrm{M}_z^{\varepsilon\,\mathrm{E(b)(k)}} \mathbf{e}_z^{\mathrm{b(k)}}\Big) \cdot \mathbf{w}^{\mathrm{E(b)}} \\
&+ \delta \Big(\mathrm{M}_x^{\varepsilon\,\mathrm{O(b)(k)}} \mathbf{e}_x^{\mathrm{b(k)}} + \mathrm{M}_y^{\varepsilon\,\mathrm{O(b)(k)}} \mathbf{e}_y^{\mathrm{b(k)}} \\
&+ \mathrm{M}_z^{\varepsilon\,\mathrm{O(b)(k)}} \mathbf{e}_z^{\mathrm{b(k)}}\Big) \cdot \mathbf{w}^{\mathrm{O(b)}}\Big) \\
&+ \sum_{\mathrm{b}\in\mathbf{B}_R} \delta \left(\varepsilon\, l^b \left(\mathbf{e}_x \wedge \mathbf{F}^{\varepsilon\,\mathrm{b}}\right)\right) \cdot \mathbf{w}^{\mathrm{C(b)}} \\
&+ \sum_{\mathrm{b}\in\mathbf{B}_R} \left(\mathrm{M}^{\varepsilon\,\mathrm{E(b)(k)}} \cdot \mathbf{w}^{\mathrm{E(b)}} + \mathrm{M}^{\varepsilon\,\mathrm{O(b)(k)}} \cdot \mathbf{w}^{\mathrm{O(b)}}\right) \\
&+ \sum_{\mathrm{b}\in\mathbf{B}_R} \left(\varepsilon\, l^b \left(\mathbf{e}_x \wedge \mathbf{F}^{\varepsilon\,\mathrm{b}}\right) \cdot \mathbf{w}^{\mathrm{C(b)}}\right) = 0 \qquad (14)
\end{aligned}
$$

with $\Delta\mathbf{v} = \mathbf{v}\left(\mathrm{E_R}\left(\mathrm{b}\right)\right) - \mathbf{v}\left(\mathrm{O_R}\left(\mathrm{b}\right)\right)$ the relative virtual velocity of the two extremity nodes of any beam. Introducing the beam vector length $\mathbf{B}^{\mathrm{b}} = l^b \mathbf{e}_x^{\mathrm{b}}$ (Fig. 2) with l^b the beam length and $\mathbf{e}_x^{\mathrm{b}}$ the unit beam director, respectively the quantities $l^b = \left\|\mathbf{B}^{\mathrm{b}}\right\|$ and $\mathbf{e}_x^{\mathrm{b}} = \frac{\mathbf{B}^{\mathrm{b}}}{l^b}$.

We shall consider lattices which are much softer in bending in comparison to tension, so that we shall presently address geometrical nonlinearities, which are traduced by changes of beam orientation and length, pictured on Fig. 2.

For any $\mathrm{b} \in \mathbf{B}_{\mathrm{R}}$, the beam vector can be evaluated from the imposed transformation gradient $\mathbf{G}^{\mathrm{j}}$ and the relative position vector between the two extremity nodes, quantity $\mathbf{R}^{\mathrm{E_R(b)}} - \mathbf{R}^{\mathrm{O_R(b)}}$ as

$$
\mathbf{B}^{\mathrm{b}} = \mathbf{R}^{\mathrm{E_R(b)}} - \mathbf{R}^{\mathrm{O_R(b)}} + \mathbf{G}^{\mathrm{j}}\delta^{\mathrm{jb}} \qquad (15)
$$

Similarly, the relative microrotation is defined and expressed versus the imposed microcurvature $\mathbf{M}^{\mathrm{j}}$ as

$$
\boldsymbol{\varphi}^{\mathrm{E_{R(b)}}} - \boldsymbol{\varphi}^{\mathrm{O_{R(b)}}} = \left(\boldsymbol{\varphi}_1^{\mathrm{E_{R(b)}}} - \boldsymbol{\varphi}_1^{\mathrm{O_{R(b)}}} + \mathbf{M}^{\mathrm{j}}\delta^{\mathrm{jb}}\right) \qquad (16)
$$

The following notations have been introduced: $\mathbf{G}^{\mathrm{j}} = \frac{\partial\mathbf{R}}{\partial\beta^j}$, $\mathbf{M}^{\mathrm{j}} = \frac{\partial\boldsymbol{\varphi}_0}{\partial\beta^j}$ are respectively the imposed mesoscopic transformation gradient and microcurvature mapping over the unit cell, and $\mathbf{R}^{\mathrm{E_R(b)}} - \mathbf{R}^{\mathrm{O_R(b)}}$ and $\boldsymbol{\varphi}_1^{\mathrm{E_R(b)}} - \boldsymbol{\varphi}_1^{\mathrm{O_R(b)}}$ are the unknown kinematic relative positions and rotations that are computed incrementally, as will be explained later on.

The variation of the beam unit vectors and lengths given in Appendix 2, Eq. (37) together with the perturbed expressions of forces and moments expressed in (40) are inserted into the incremental equilibrium (14); this entails the identification and extraction of the total tangent stiffness matrix, which in turn is divided to the stress stifness $\left(\mathbf{K}_{\mathrm{T}}^{\mathrm{S}}\right)$ and the micropolar stiffness $\left(\mathbf{K}_{\mathrm{T}}^{\mathrm{m}}\right)$. We observe that the tangent stress stiffness leads to identify three type of stiffness matrices $\mathbf{K}_{\mathrm{So}}, \mathbf{K}_{\mathrm{u}}, \mathbf{K}_{\sigma}$, respectively the linear stiffness matrix, the initial displacement stiffness matrix and initial stress stiffness matrix, given in Appendix 2. The tangent stress stiffness accordingly decomposes additively as

$$
\mathbf{K}_{\mathrm{T}}^{\mathrm{S}} = \sum_{\mathrm{b}\in\mathbf{B}_{\mathrm{R}}} \left(\mathbf{K}^{\mathrm{b}}{}_{\mathrm{So}} + \mathbf{K}_{\mathrm{u}}^{\mathrm{b}} + \mathbf{K}_{\sigma}^{\mathrm{b}}\right) \qquad (17)
$$

For the micropolar nonlinear response, the tangent stiffness matrix similarly decomposes additively as

$$
\mathbf{K}_{\mathrm{T}}^{\mathrm{m}} = \sum_{\mathrm{b}\in\mathbf{B}_{\mathrm{R}}} \left(\mathbf{K}_{\mathrm{mo}}^{\mathrm{b}} + \mathbf{K}_{\mathrm{m}}^{\mathrm{b}}\right) \qquad (18)
$$

with $\mathbf{K}_{\mathrm{mo}}^{\mathrm{b}}$ the initial micropolar stiffness matrix and $\mathbf{K}_{\mathrm{m}}^{\mathrm{b}}$ the tangent micropolar stiffness matrix, both expressed in Appendix 2.

Now the left-hand side of equations (15, 16) includes both the imposed mesoscopic transformation gradient $\mathbf{G}^{\mathrm{j}} = \frac{\partial\mathbf{R}}{\partial\beta^j}$ and microcurvature mapping $\mathbf{M}^{\mathrm{j}} = \frac{\partial\boldsymbol{\varphi}_0}{\partial\beta^j}$ over the unit cell, and the unknown kinematic quantities $\mathbf{R}^{\mathrm{E_R(b)}} - \mathbf{R}^{\mathrm{O_R(b)}}$ and $\boldsymbol{\varphi}^{\mathrm{E_R(b)}} - \boldsymbol{\varphi}^{\mathrm{O_R(b)}}$. The solution for these differences is obtained by solving iteratively previous incremental scheme based on the modified Newton–Raphson method.

This incremental scheme provides an update for the kinematic variables $\mathbf{B}^{\mathrm{b(k+1)}}$, $\boldsymbol{\varphi}^{\mathrm{b(k+1)}}$ at any iteration $(\mathrm{k}+1)$, from their values at previous iteration k within the reference unit cell: for a given imposed mesoscopic transformation gradient and microcurvature, respectively the variables $\mathbf{G}^{\mathrm{j}}$, $\mathbf{M}^{\mathrm{j}}$, the update of the position and microrotation vectors is written as

$$
\begin{aligned}
\mathbf{B}^{\mathrm{b(k+1)}} &= \mathbf{B}^{\mathrm{b(k)}} + \delta\,\mathbf{B}^{\mathrm{b(k)}},\ \text{with}\ \ \mathbf{B}^{\mathrm{b(k)}} = \mathbf{R}^{\mathrm{E_R(b)(k)}} \\
&\quad - \mathbf{R}^{\mathrm{O_R(b)(k)}} + \mathbf{G}^{\mathrm{j}}\delta^{\mathrm{jb}} \\
\boldsymbol{\varphi}^{\mathrm{b(k+1)}} &= \boldsymbol{\varphi}^{\mathrm{b(k)}} + \delta\,\boldsymbol{\varphi}^{\mathrm{b(k)}},\ \text{with}\ \boldsymbol{\varphi}^{\mathrm{b(k)}} \\
&= \boldsymbol{\varphi}^{\mathrm{E_R(b)(k)}} - \boldsymbol{\varphi}^{\mathrm{O_R(b)(k)}} + \mathbf{M}^{\mathrm{j}}\delta^{\mathrm{jb}} \qquad (19)
\end{aligned}
$$

For a given kinematic loading over the RUC described by $\frac{\partial\mathbf{R}}{\partial\beta^j}\delta^{jb}$, $\frac{\partial\boldsymbol{\varphi}}{\partial\beta^j}\delta^{jb}$, $j = 1, 2, 3$, one can determine the quantities $\mathbf{B}^b, \mathbf{e}_x^b, \mathbf{e}_y^b, \mathbf{e}_z^b, F_x^b, F_y^b, F_z^b, M_x^b, M_y^b, M_z^b$, for any $b \in \mathbf{B}_R$, allowing to calculate the stress and the couple stress vectors $\mathbf{S}^i$ and $\boldsymbol{\mu}^i$ respectively.

The mesoscopic incremental equations are next written at the continuum level of the RUC.

2.2.2 Mesoscopic field equations over the reference unit cell

As an extension of the small perturbation equilibrium, the discrete incremental equilibrium takes after homogenization a form similar to its continuum counterpart, viz it holds

$$\sum_{\upsilon^i \in \mathbb{Z}^3} \sum_{\mathrm{b} \in \mathbf{B}_\mathrm{R}} \delta \mathbf{F}^\mathrm{b} \cdot \mathbf{v}^\varepsilon + \sum_{\upsilon^i \in \mathbb{Z}^3} \sum_{\mathrm{b} \in \mathbf{B}_\mathrm{R}} \delta \mathbf{M}^\mathrm{b} \cdot \mathbf{W}^\varepsilon = 0$$
$$\Rightarrow \int_\Omega \delta \mathbf{S}^{\mathrm{i(k)}} \cdot \frac{\partial \mathbf{v}}{\partial \beta^\mathrm{i}} d\beta + \int_\Omega \delta \boldsymbol{\mu}^{\mathrm{i(k)}} \cdot \frac{\partial \mathbf{w}}{\partial \beta^\mathrm{i}} d\beta = 0 \qquad (20)$$

with $\delta \mathbf{S}^{\mathrm{i(k)}}$ and $\delta \boldsymbol{\mu}^{\mathrm{i(k)}}$ the incremental stress and couple stress vectors; previous integral formulation constitutes the incremental weak form of the equilibrium (self-equilibrium) posed over the Lagrangian domain Ω occupied by the reference unit cell.

We next aim at writing the incremental constitutive law at the mesoscopic level. We first recall a few needed notations from nonlinear continuum mechanics. A generic particle occupies a reference position $\mathbf{X}$. When the body deforms due to prescribed tractions or displacements, the spatial position of the particle originally at $\mathbf{X}$ is given by $\mathbf{x} = \mathrm{f}(\mathbf{X})$, with function f supposed to be a smooth one-to-one point mapping. The displacement $\mathbf{u}(\mathbf{X})$of the particle is defined by $\mathbf{u}(\mathbf{X}) = \mathrm{f}(\mathbf{X}) - \mathbf{X}$, and the deformation gradient elaborated as $\mathbf{F}(\mathbf{X}) = \nabla \mathrm{f}(\mathbf{X})$.

We shall applied kinematic-controlled loadings over the unit cell, we shall impose at each increment the discretized version of $\mathbf{F}$, or the microcurvature, which is specific to each type of loading. We shall subsequently investigate the response of lattices under uniaxial tension, equibiaxial tension, simple shear, and bending. The kinematic load parameter is started at zero value and incremented, and the equilibrium solution is computed at each increment; we shall in the sequel denote n the step number.

We shall in the sequel and in view of setting up the incremental scheme for the resolution of the nonlinear mesoscopic BVP (acronym for boundary value problem) write the discretized version of the elastic constitutive equation successively between the incremental stress $\Delta \mathbf{S}_\mathrm{n}^{(\mathrm{k})}$ and the incremental strain $\Delta \mathbf{E}_{\mathrm{Gn}}^{(\mathrm{k})}$, and between the incremental couple stress $\Delta \mathbf{M}_\mathrm{n}^{(\mathrm{k})}$ and incremental curvature tensor $\Delta \boldsymbol{\Gamma}_\mathrm{n}^{(\mathrm{k})}$ (these two increments are in fact imposed over the RUC), as

$$\Delta \mathbf{S}_\mathrm{n}^{(\mathrm{k})} = \mathrm{K}_{\mathrm{T,n}}^{\mathrm{S}} : \Delta \mathbf{E}_{\mathrm{Gn}}^{(\mathrm{k})}$$
$$\Delta \mathbf{M}_\mathrm{n}^{(k)} = \mathrm{K}_{\mathrm{T,n}}^{\mathrm{m}} : \Delta \boldsymbol{\Gamma}_\mathrm{n}^{(\mathrm{k})} \qquad (21)$$

The Green–Lagrange strain ($\mathbf{E}_\mathrm{G}$) therein is defined by $\mathbf{E}_\mathrm{G} = \frac{1}{2}\left(\mathbf{F}^\mathbf{T} \cdot \mathbf{F} - \mathrm{I}\right)$. The stress tangent stiffness matrix $\mathbf{K}_{\mathrm{T,n}}^{\mathrm{S}}$ results from the assembly of the microscopic tangent stiffness matrices, and is computed at each increment.

We further express the Lagrangian wryness tensor $\boldsymbol{\Gamma}$as the following second order tensor versus the finite rotation vector $\boldsymbol{\varphi} = \varphi_i \mathbf{e}_i$ [30]

$$\boldsymbol{\Gamma} = \nabla_X \boldsymbol{\varphi} \left[\frac{\sin\left(\|\boldsymbol{\varphi}\|\right)}{\|\boldsymbol{\varphi}\|} \mathrm{I} - \frac{1 - \cos\left(\|\boldsymbol{\varphi}\|\right)}{\|\boldsymbol{\varphi}\|^2} \boldsymbol{\varphi} \times \mathbf{I} \right.$$
$$\left. + \frac{\|\boldsymbol{\varphi}\| - \sin\left(\|\boldsymbol{\varphi}\|\right)}{\|\boldsymbol{\varphi}\|^3} \boldsymbol{\varphi} \otimes \boldsymbol{\varphi} \right] \qquad (22)$$

denoting therein ∇_X the gradient operator with respect to the Lagrangian coordinate $\mathbf{X}$. For a given elementary loading characterized by a continuously varying scalar loading parameter λ_n, the incremental Lagrangian strain $\Delta \mathbf{E}_{\mathrm{Gn}}$ is related to the increment of the loading parameter λ_n and the increment $\Delta \mathbf{F}_\mathrm{n}$ as in [31]

$$\Delta \mathbf{E}_{\mathrm{Gn}}(\lambda_\mathrm{n}, \Delta\lambda_\mathrm{n}) = \mathrm{sym}\left(\mathbf{F}_\mathrm{n}\left(\lambda_\mathrm{n}\right)^\mathrm{T} \cdot \nabla_\mathrm{X} \Delta \mathbf{u}_\mathrm{n}\right)$$
$$\equiv \mathrm{sym}\left(\mathbf{F}_\mathrm{n}\left(\lambda_\mathrm{n}\right)^\mathrm{T} \cdot \Delta \mathbf{F}_\mathrm{n}\left(\Delta\lambda_\mathrm{n}\right)\right) \qquad (23)$$

together with the relation

$$\mathbf{F}_\mathrm{n}\left(\lambda_\mathrm{n}\right) = \mathbf{I} + \nabla_\mathrm{X} \mathbf{u}_\mathrm{n} \rightarrow \Delta \mathbf{F}_\mathrm{n}\left(\Delta\lambda_\mathrm{n}\right) = \Delta \nabla_\mathrm{X} \mathbf{u}_\mathrm{n} \equiv \nabla_\mathrm{X} \Delta \mathbf{u}_\mathrm{n} \qquad (24)$$

We recall that the stress increment $\Delta \mathbf{S}_\mathrm{n}^{(\mathrm{k})}$ expresses versus the strain increment $\Delta \mathbf{E}_{\mathrm{Gn}}$ according to Eq. (21).

The updated Cauchy stress tensor is next obtained by a push-forward of the incremental Lagrangian stress $\Delta \mathbf{S}_\mathrm{n}^{(\mathrm{k})}$ from configuration Ω_n to $\Omega_{\mathrm{n}+1}$, elaborated as

$$\boldsymbol{\sigma}_{\mathrm{n}+1}^{(\mathrm{k})} = \underbrace{\left(\mathrm{J}_\mathrm{n}^{-1} \mathbf{F}_\mathrm{n} \cdot \mathbf{S}_\mathrm{n}^{(\mathrm{k})} \cdot \mathbf{F}_\mathrm{n}^\mathrm{T}\right)}_{\boldsymbol{\sigma}_\mathrm{n}^{(\mathrm{k})}} + \underbrace{\left(\mathrm{J}_\mathrm{n}^{-1} \mathbf{F}_\mathrm{n} \cdot \left(\Delta \mathbf{S}_\mathrm{n}^{(\mathrm{k})}\right) \cdot \mathbf{F}_\mathrm{n}^\mathrm{T}\right)}_{\Delta \boldsymbol{\sigma}_\mathrm{n}^{(\mathrm{k})}} \qquad (25)$$

where $\mathrm{J} = \det(\mathbf{F})$ is the Jacobian, defined as the determinant of the deformation gradient tensor. A subscript k refers to the iteration index which is inside the increment loop. The Cauchy stress at increment n + 1 is accordingly given from its counterpart at previous increment n, based on the initial stress $\mathbf{S}_\mathrm{n}^{(\mathrm{k})}$ (the first contribution on the right-hand side of (25)) and the incremental stress $\Delta \boldsymbol{\sigma}_\mathrm{n}^{(\mathrm{k})}$ (the second term on the right-hand side).

In order to get an update for the incremental couple stress tensor, one has to exploit a similar relation previously derived for the Cauchy stress.

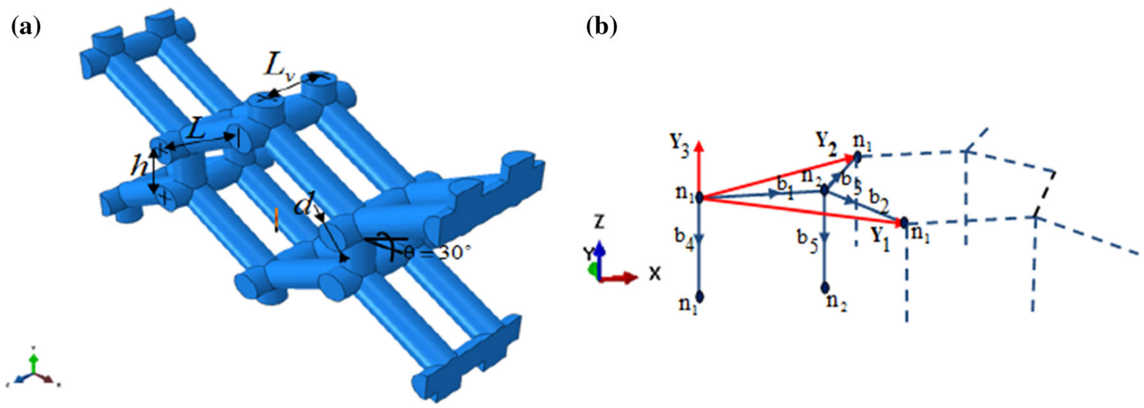

Fig. 3 3D hexagonal lattice **a** geometric description of the repeatable unit cell and **b** the representative unit cell

$$\mathbf{m}_{n+1}^{(k)} = \underbrace{\left(\overline{\mathbf{R}}_n \cdot \mathbf{M}_n^{(k)} \cdot \mathbf{F}_n^T\right)}_{\mathbf{m}_n^{(k)}} + \underbrace{\left(\overline{\mathbf{R}}_n \cdot \left(\Delta \mathbf{M}_n^{(k)}\right) \cdot \mathbf{F}_n^T\right)}_{\Delta \mathbf{m}_n^{(k)}} \qquad (26)$$

where $\overline{\mathbf{R}}_n$ is the micropolar rotation tensor at increment n, defined as $\overline{\mathbf{R}}_n = \exp(\mathrm{spn}(\boldsymbol{\varphi}))$ and expressed in closed form by using the Euler–Rodrigues formula, as explained in [32].

Within a specified type of loading (imposed transformation gradient or microcurvature over the unit cell), one has to determine the adequate macroscopic displacement boundary conditions that have to be imposed over the RUC; this is next done for uniaxial tension, simple shear, equibiaxial tension, and bending considered as elementary loadings.

Moreover, the characteristic lengths for bending of the micropolar effective nonlinear continuum are further evaluated from both the effective classical and micropolar tangent stiffness matrices, relying on the linear situation. The internal lengths are then computed at each increment of the scheme. An example shall be given later on in this contribution.

2.3 Algorithm of the homogenization method

In a first step, the homogenized constitutive law is evaluated in the linear framework. As a next step, one set up a kinematic driven algorithm by which, for each load increment, the incremental stress and couple stress tensors are computed versus the imposed mesoscopic loading (transformation gradient and microcurvature). The evolution of the kinematic and static quantities follows the update of the lattice geometry.

A dedicated code has been constructed from the proposed algorithm, in order to solve for the nodal kinematical unknowns (displacements and microrotations) of each beam within the repetitive unit cell. The code relies on an input file the initial reference unit cell topology and mechanical properties, and delivers as an output the homogenized mechanical properties (classical and micropolar moduli) and stress–strain response for a given deformation path; the response is computed more specifically for each of the aforementioned elementary loadings, as explained in Box 1.

The implementation of the algorithm for the solution of both the linear and nonlinear problems has been done in symbolic language giving rise to a dedicated Maple code.

The next sections are devoted to different examples to illustrate the proposed computational method; we will compute the nonlinear mechanical response of the 3D hexagonal lattice, followed by dry textile structures for 2D and 3D geometries.

3 Numerical examples

3.1 3D hexagonal lattice

A mechanical analysis of a general 3D anisotropic hexagonal lattice with in-plane struts of length L and h and vertical struts of length L_v (out-of-plane) is considered, both endowed with circular cross-section of diameter d (Fig. 3a). The whole lattice is generated from the repetition of the unit cell shown in Fig. 3b thanks to three periodicity vectors defined in the Cartesian basis. This geometry is representative of the unit cell of vertebral trabecular bone. The length of the periodicity vectors $\mathbf{Y}_1, \mathbf{Y}_2, \mathbf{Y}_3$ in the Cartesian basis are $L_1 = L_2 = \sqrt{(L\cos\theta)^2 + (h + L\sin\theta)^2}$ and $L_3 = L_v$.

The considered hexagonal unit cell is composed of five beams: three horizontal beams b_1, b_2, and b_3 and the vertical beams b_4 and b_5. Beams b_2 and b_3 have the same length L and are inclined by the angle $\theta = 30°$ towards the horizontal direction, while beam b_1 has length h. The vertical beams b_4 and b_5 have the same length L_v. The connectivity Table 1 gives the numbering of beams and nodes within the chosen representative unit cell.

We consider to be specific a hexagonal unit cell pictured in Fig. 3 with the following geometrical parameters: d = 0.25 mm, L = 1 mm, L_v = 0.5 mm, h = 0.5 mm, and $\theta = 30°$;

Box 1 Algorithm for the nonlinear discrete homogenization of repetitive lattices

For each kinematic increments $\Delta\mathbf{E}_{\mathrm{Gn}}^{(\mathrm{k})}$, $\Delta\boldsymbol{\Gamma}_{\mathrm{n}}^{(\mathrm{k})}$;

For each iteration k inside the increment loop;

1. Compute the effective mechanical properties in the linear regime based on the linear discrete homogenization framework, Eq. (12).
2. Define the incrementally imposed strain and microcurvature applied over the RUC.
3. Compute the incremental Second Piola-Kirchhoff stress tensor and couple stress tensor, Eq. (21),
$$\Delta\mathbf{S}_{\mathrm{n}}^{(\mathrm{k})} = \mathrm{K}_{\mathrm{T,n}}^{\mathrm{S}} : \Delta\mathbf{E}_{\mathrm{Gn}}^{(\mathrm{k})}$$
$$\Delta\mathbf{M}_{\mathrm{n}}^{(\mathrm{k})} = \mathrm{K}_{\mathrm{T,n}}^{\mathrm{m}} : \Delta\boldsymbol{\Gamma}_{\mathrm{n}}^{(\mathrm{k})}$$
4. Check convergence at iteration k; if it is attained, go to next step.
5. Compute the incremental deformation gradient, Eq. (24), and its Jacobian.
6. Update Cauchy stress and couple stress at increment $(n+1)$, by a push forward of their Lagrangian counterpart from Ω_n to Ω_{n+1}, Eqs. (25) and (26):
$$\boldsymbol{\sigma}_{\mathrm{n+1}}^{(\mathrm{k})} = \mathrm{J}_{\mathrm{n}}^{-1}\mathbf{F}_{\mathrm{n}} \cdot \left\{\mathbf{S}_{\mathrm{n}}^{(\mathrm{k})} + \Delta\mathbf{S}_{\mathrm{n}}^{(\mathrm{k})}\right\} \cdot \mathbf{F}_{\mathrm{n}}^{\mathrm{T}} = \underbrace{\left(\mathrm{J}_{\mathrm{n}}^{-1}\mathbf{F}_{\mathrm{n}} \cdot \mathbf{S}_{\mathrm{n}}^{(\mathrm{k})} \cdot \mathbf{F}_{\mathrm{n}}^{\mathrm{T}}\right)}_{\boldsymbol{\sigma}_{\mathrm{n}}^{(\mathrm{k})}} + \underbrace{\left(\mathrm{J}_{\mathrm{n}}^{-1}\mathbf{F}_{\mathrm{n}} \cdot \left(\Delta\mathbf{S}_{\mathrm{n}}^{(\mathrm{k})}\right) \cdot \mathbf{F}_{\mathrm{n}}^{\mathrm{T}}\right)}_{\Delta\boldsymbol{\sigma}_{\mathrm{n}}^{(\mathrm{k})}}$$
$$\mathbf{m}_{\mathrm{n+1}}^{(\mathrm{k})} = \underbrace{\left(\overline{\mathbf{R}}_{\mathrm{n}} \cdot \mathbf{M}_{\mathrm{n}}^{(\mathrm{k})} \cdot \mathbf{F}_{\mathrm{n}}^{\mathrm{T}}\right)}_{\mathbf{m}_{\mathrm{n}}^{(\mathrm{k})}} + \underbrace{\left(\overline{\mathbf{R}}_{\mathrm{n}} \cdot \left(\Delta\mathbf{M}_{\mathrm{n}}^{(\mathrm{k})}\right) \cdot \mathbf{F}_{\mathrm{n}}^{\mathrm{T}}\right)}_{\Delta\mathbf{m}_{\mathrm{n}}^{(\mathrm{k})}}$$
7. Update the network configuration from Ω_{n} to $\Omega_{\mathrm{n+1}}$.
8. Repeat steps 1–7 up to the maximum applied strain and curvature over the unit cell.

Table 1 Connectivity array for the 3D hexagonal lattice

Beam	1	2	3	4	5
O (b)	1	2	2	1	2
O (b)	2	1	1	1	2
δ_1	0	1	0	0	0
δ_2	0	0	1	0	0
δ_3	0	0	0	−1	−1

Young's modulus and Poisson's ratio of the cell wall material are selected as $\mathrm{E_s} = 12{,}000$ MPa $\nu_{\mathrm{s}} = 0.3$.

We next plot the nonlinear elastic responses in terms of the components of Cauchy stress versus the stretches for different types of loading. Figure 4 shows the nonlinear response in terms of the evolution of the Cauchy stress diagonal components versus the stretch applied in the three corresponding directions x, y and z. The comparison with the extrapolated linear response highlights a strong nonlinear response for tension along x, and a less pronounced nonlinear response for tension along the two other directions. The response under tension in z-direction shows a nearly linear behaviour followed by a light softening (see Fig. 4c).

The responses under equi-biaxial tension show a nearly linear evolution of Cauchy stress components versus stretch for both x and y directions, as shown in Fig. 5.

The shear stress response shows an important difference between the linear and geometrical nonlinear analysis beyond about 10 % shear strain (Fig. 6), due to a large change in the beam director orientation during shear, contrary to the equi-biaxial test.

We next compute the nonlinear response of textile dry preforms which exhibit strong geometrical nonlinearities. Many modeling approaches have been used to analyze the mechanical behavior of fabrics, which can be classified into analytical and numerical models. A lot of mesostructurally based analytical models have been developed for the study of the behavior of woven fabrics [1] and references therein. The literature review [33,34] shows that finite element analyses and analytical methods are powerful tools for studying the mechanical properties of woven fabrics. However, the complexity of the micro-structure is proportional to the number of parameters controlling the mechanical properties. Consequently, various assumptions should be proposed to simplify the analysis.

3.2 Nonlinear response of textile monolayers

We consider to be specific textile monolayer fabrics patterns, viz plain weave and twill as representative examples of 2D preforms. The RUC of the fabric is constructed and modeled as a network of trusses connected by nodes at cross points of the interwoven yarns within the fabric. These trusses have extensional and bending rigidities to represent yarn stretching and flexion. The contact interactions between yarns at the cross-over points are captured by beam segments connecting the nodes. The proposed methodology has been used for the analysis of plain weave and twill fabrics subjected to large applied strains. The stress–strain responses are evaluated after applying appropriate boundary condition to the

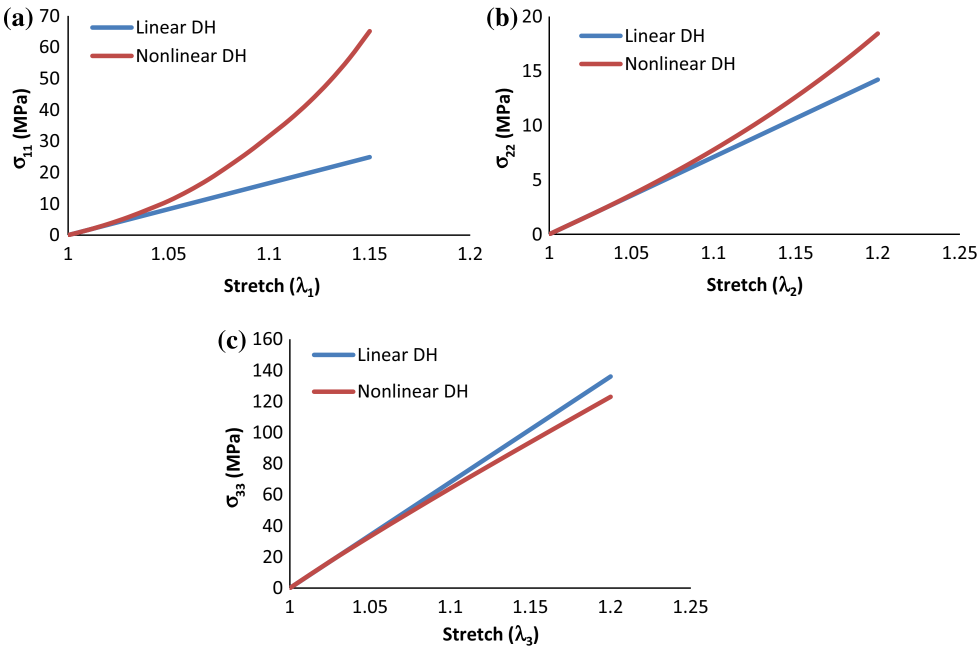

Fig. 4 Evolution of Cauchy stress components versus the corresponding applied stretch under uniaxial tension of the 3D hexagon in **a** x-direction, **b** y-direction and **c** z-direction

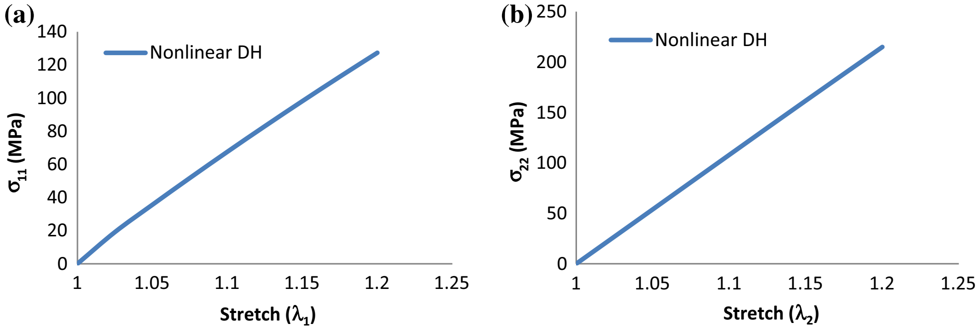

Fig. 5 Equi-biaxial tensile Cauchy stress versus stretch for the 3D hexagon in **a** x-direction and **b** y-direction

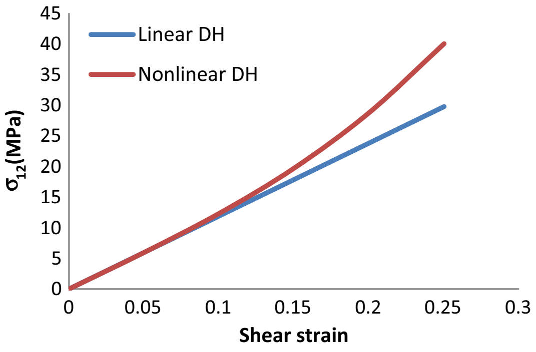

Fig. 6 Nonlinear in-plane shear stress response versus applied shear strain for the 3D hexagon

RUC, considering the previous three elementary loading cases, namely uniaxial tension, bi-axial tension and simple shear.

Most of the models for woven fabrics are based on the definition of the unit cell geometry and include the major architectural parameters for predicting the mechanical properties. The unit cell is selected as the smallest unit of textile that, when tiled, will generate the full scale textile. The initial geometry of the unit cell is modeled using TexGen, a free and open source license software, operating on Windows and Linux, and developed for the purpose of research on technical textiles at the University of Manchester (www.texeng.co.uk). Two typical textile patterns are considered in the present work, plain weave and twill fabrics (Fig. 7). Modeling of this architecture is relatively tedious with conventional CAD, so we instead use TexGen in order to save time in the generation of the geometrical model and to export the geometric files to ABAQUS where the finite element analysis is subsequently done.

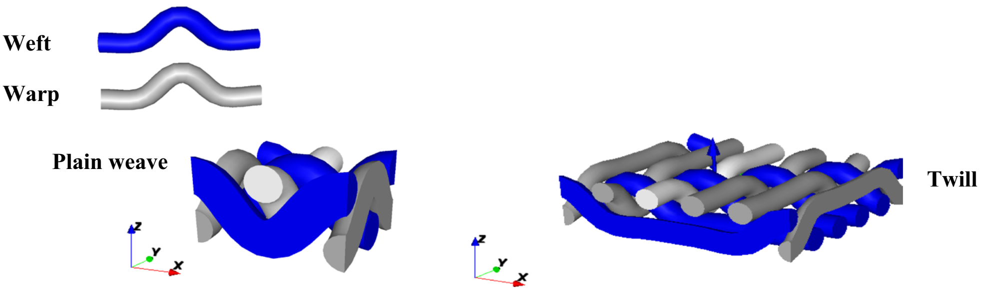

Fig. 7 Representative plain weave and twill unit cells

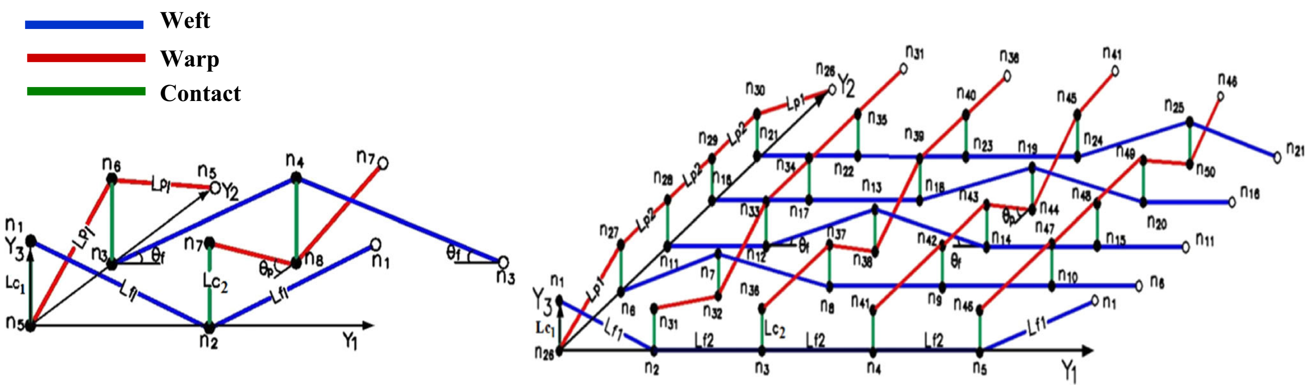

Fig. 8 Geometric description for the unit cell of plain weave (*left*) and twill (*right*)

The RUC of the fabric is constructed and modeled as a network of trusses connected by nodes at cross points of the interwoven yarns within the fabric. For the two chosen applications of (a) plain weave (b) twill, the proposed geometrical description for the unit cell of fabric and the corresponding periodicity vectors are represented on Fig. 8. The geometrical and mechanical parameters of these two structures are given in Appendix 3.

Small strain discrete homogenization schemes were recently developed by Goda et al. [1] for the determination of the effective mechanical properties of textiles monolayers, with the stiffness matrix components expressed versus the material and microstructural geometric parameter. The discrete homogenization approach as explained in Sect. 2 has been implemented for the two types of fabric. The analyses of the periodic reinforcements modelled as RUC have been implemented within a dedicated code considering the impact of a variation of the structure geometry simultaneously in a nested manner.

A comparison between the mechanical response of plain weave and twill is next performed under three types of loading (uniaxial tension, biaxial tension and simple shear).

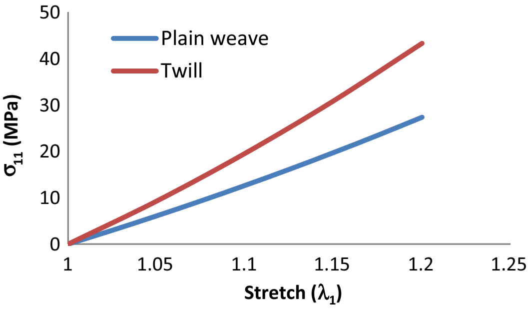

Fig. 9 Cauchy stress evolution versus stretch for plain weave and twill under a uniaxial tensile loading

- *Uniaxial tension* Figure 9 shows a comparison between the Cauchy stress response versus stretch under a uniaxial tensile loading test, for both plain weave and twill.

  The initial homogenized tensile rigidity in the weft direction are 113.5 and 170.4 MPa for plain weave and twill respectively. The stiffest response obtained for twill can be explained by the fact that yarns within the representative unit cell are more aligned in the direction in traction; we expect this tendency to be valid for any loading.
- *Biaxial tension* The biaxial tensile strain simulation is realized by applying a strain in the longitudinal direction of warp and weft yarns; we shall define the biaxial strain ratio $\varepsilon_2/\varepsilon_1$, where ε_1 is the primary textile strain corresponding to weft direction, and ε_2 is the secondary strain corresponding to the warp direction. Figure 10 shows the comparison of the biaxial response for plain weave and

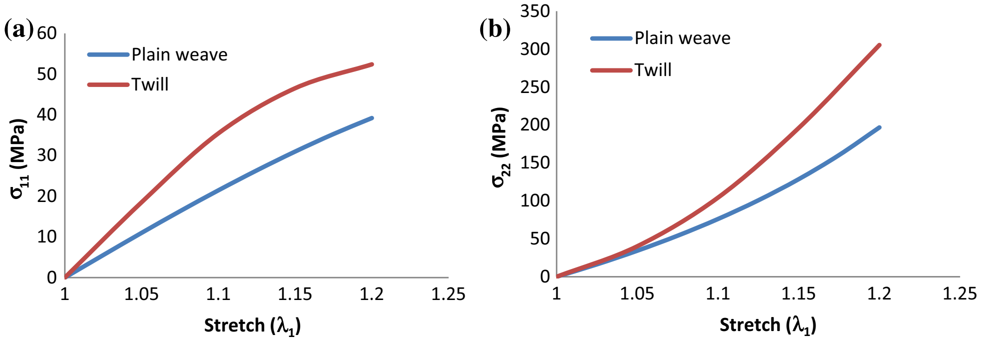

Fig. 10 Comparison between Cauchy stress evolutions versus stretch for plain weave and twill in **a** x-direction and **b** y-direction

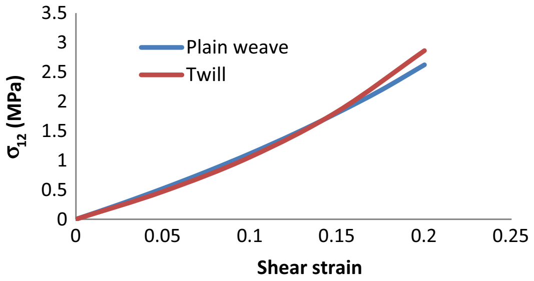

Fig. 11 Comparison between the shear response for plain weave and twill

twill for a biaxial ratio equal to two: twill shows as for uniaxial tension a stiffer response.

- *Simple shear test* The shear response shows nearly the same trend for both types of fabrics up to a shear strain of 0.15, with a small difference occurring for large strains, as shown in Fig. 11; this can be explained by the fact that the initial yarn crimp does not play an important role in simple shear (contrary to uniaxial loading conditions).
- *Bending test* Bending is applied to the twill structure by imposing an increasing microcurvature over the unit cells; the incremental bending response is then computed based on the incremental scheme exposed in Sect. 2. Note that although we perform a pure bending test, we need to solve both the equilibrium equation of forces and moments (see Fig. 12). Since we shall focus on bending applied along one coordinate axis, a straightforward computation shows that the Lagrangian wryness expressed in (22) simplifies to $\mathbf{\Gamma} = \mathrm{Grad}\,(\boldsymbol{\varphi})$. We compute as an illustration the flexural response (out-of-plane bending) of twill performed over its representative unit cell shown on Fig. 8. The small bending stiffness which is needed to initiate the nonlinear bending computations is related to the linearized curvature ($\chi_{xy} = \partial\varphi_y/\partial x$) by

$$m_{xy} = K^m_{T,xy}\,\chi_{xy} \tag{27}$$

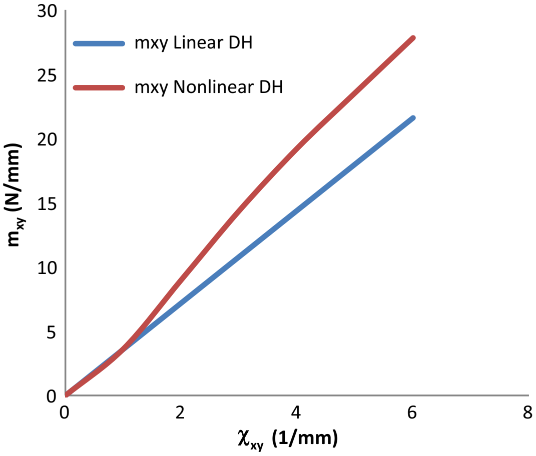

Fig. 12 Nonlinear and linear evolutions of the couple stress versus microcurvature for twill

The internal bending length for twill is evaluated from the computed effective rigidities by the expression built from the ratio of the tangent bending modulus to the sum of the corresponding tangent shear moduli,

$$l_c = \sqrt{\left(K^m_{T,xy}/2\left(K^S_{T,xz} + K^S_{T,yz}\right)\right)}; \tag{28}$$

it shows a linear increase versus the applied curvature (Fig. 13). The components of the tangent stiffness therein evolve versus the imposed curvature based on the effective constitutive law under bending, relation (27).

The next section is devoted to the computation of the large strains response of 3D textile preforms.

3.3 Large strain response of 2.5D layer-to-layer interlock

The homogenization scheme is quite general and versatile enough to be applicable for any networks having a periodical architecture. In view of this generalization, a 3D textile multilayer is analyzed. We consider as specific structures tex-

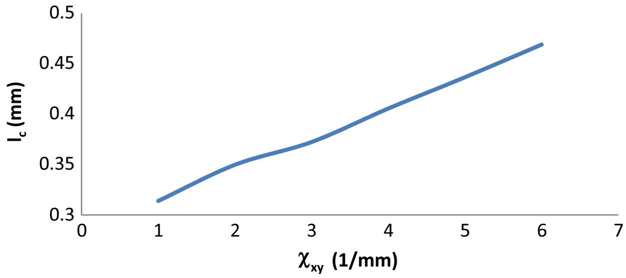

Fig. 13 Characteristic length evolution versus curvature for twill

tile multilayer fabrics patterns, viz 2.5D layer-to-layer angle interlock. In the same manner, a RUC of the fabric is constructed and modeled as a network of trusses connected by nodes at cross points of the interwoven yarns within the fabric (Fig. 14).

Warp yarns are undulated through the successive layers of weft yarns. They can be bound to different depths where various arrangement of yarns placement can be used to produce a wide range of this type of interlock. The material data for the plain weave and twill, which are used to define the material parameter for the 2.5D interlock RUC, are provided in Appendix 3. The entire geometry of the unit cell is constructed based on the geometrical parameters as summarized in the Table 2.

We next employ the proposed discrete homogenization method to analyze the deformation of the 2.5D layer-to-layer interlock subjected to uniaxial and equibiaxial loading tests. In the same manner, we plot the Cauchy stress component versus the corresponding stretch. Uniaxial tension in warp direction shows an important difference between the linear and the geometrical nonlinear analyses (Fig. 15).

Table 2 2.5D layer to layer interlock yarn geometrical parameters

	Width (mm)	Thickness (mm)
Weft	0.25	0.15
Warp	0.25	0.15

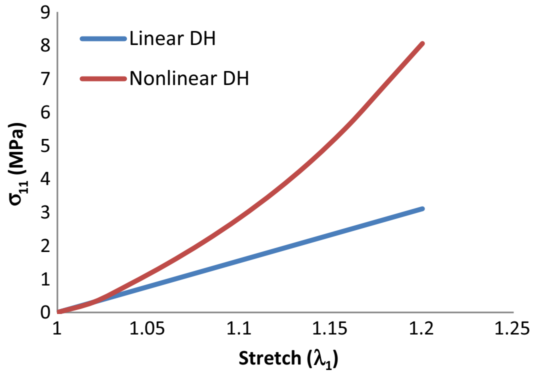

Fig. 15 Cauchy stress versus stretch for 2.5D layer to layer interlock

The response under equibiaxial tension is pictured on Fig. 16, in terms of the evolution of Cauchy stress components along x and y.

The pronounced nonlinearity of the response along x reflects the change of crimp of the yarn which tends to align in this direction as the stretch level is increased (for both uniaxial and biaxial tension); on the opposite, since the transverse yarn is initially straight, it does not produce geometrical nonlinearities, as one can infer from the rather linear response observed in Fig. 16b. This behaviour clearly illustrates geometrical nonlinearities present in these textile structures.

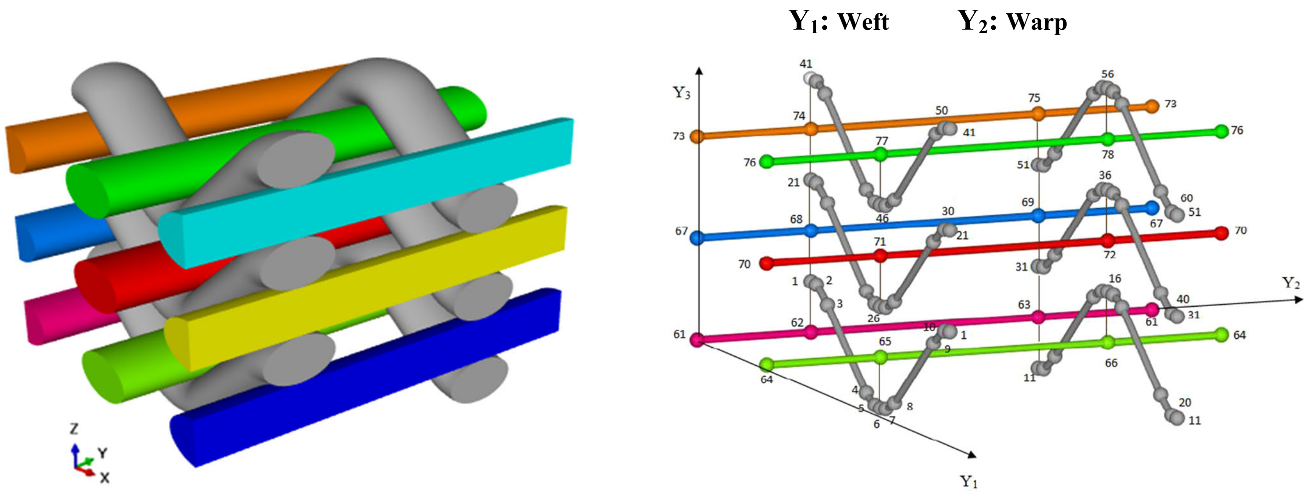

Fig. 14 Schematic representations on TexGen of 2.5D angle interlock: layer-to-layer RUC (*left*) and Geometrical model of an elementary cell (*right*)

Fig. 16 Cauchy stress in **a** x-direction and **b** y-direction versus stretch for the 2.5D layer to layer interlock

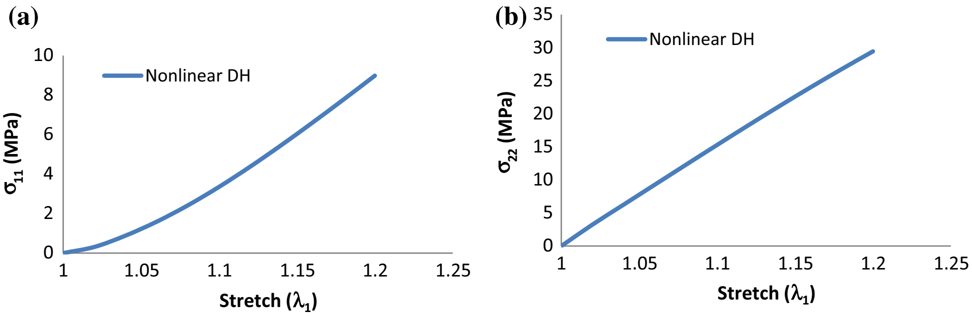

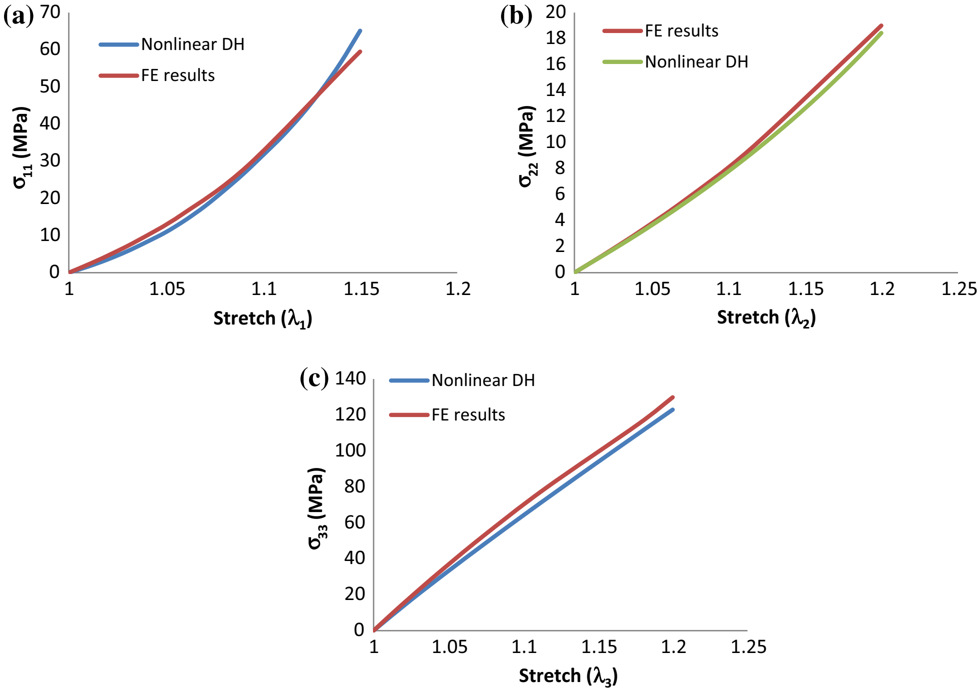

Fig. 17 Comparison of the tensile response based on discrete homogenization and finite element method in **a** x-direction, **b** y-direction and **c** z-direction

4 Comparison of the homogenized responses with FE simulations

We here demonstrate the usefulness of the unit cell approach in finite element analyses to compute the uniaxial, biaxial, and shear mechanical responses accounting for large configuration changes. A comparison to finite element results aims to evaluate the effectiveness and accuracy of the discrete homogenization approach. The finite element method consists in determining the overall effective nonlinear mechanical response over a representative unit cell of the considered structure, relying on a FE discretization of the unit cell geometry. It is possible in ABAQUS to define a problem as a “large-displacement” analysis, which means that geometric nonlinearity is accounted for in the element calculations. For each step in the analysis, we indicate whether ABAQUS will account for nonlinear effects from large displacements and deformations. If the displacements in a model due to loading are relatively small during a step, the effects may be small enough to be ignored. However, in cases where the loads on a model result in large displacements, nonlinear geometric effects can become important.

We validate the homogenized responses previously obtained for the considered structures (3D hexagon, plain weave, twill, 2.5D interlock) by comparing the evolution of stresses with those obtained thanks to FE computations performed over the corresponding representative unit cell.

4.1 Validation of the homogenization method for the 3D hexagonal structure

The effective uniaxial responses under tension (in x, y and z-directions), shear, and biaxial tension (in x–y plane) are evaluated using displacement boundary conditions, as pictured in Figs. 17, 18 and 19. The unit cell of the 3D hexagon pictured in Fig. 3 has been meshed by C3D10 elements, a 10-

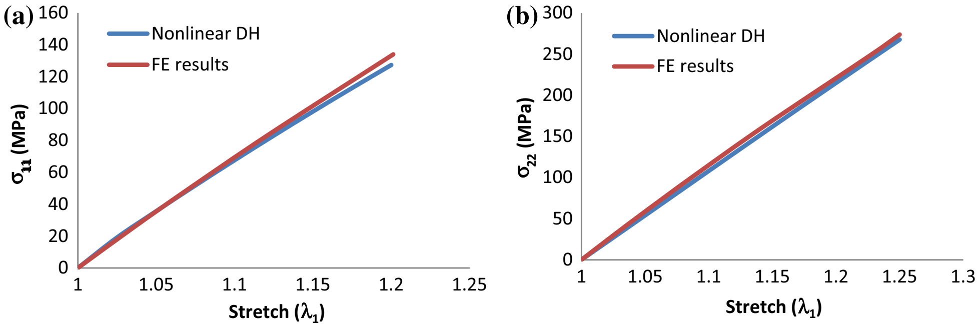

Fig. 18 Comparison of the equi-biaxial tensile stress response based on discrete homogenization and finite element method

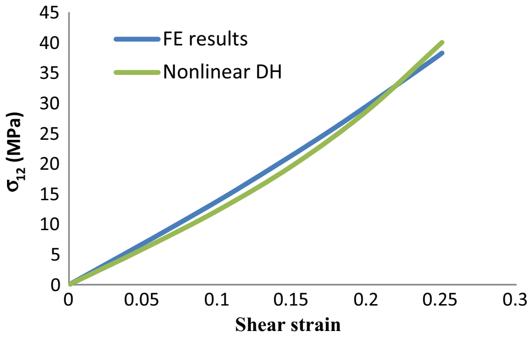

Fig. 19 Nonlinear response for the shear stress versus shear strain compared with FE results

nodes quadratic tetrahedral finite element used in ABAQUS environment. The analysis has been performed using a nonlinear perturbation analysis.

The uniaxial tensile responses in x, y and z directions are determined using displacement boundary conditions; the edge nodes are displaced by a specified amount while the nodes on the opposite edge are prevented from any translation in the displacement direction. The nodes located at one of the two opposite sides in the direction normal to the displacement direction are prevented from translation in the direction normal to the displacement direction. The stress–stretch curves are then constructed from the reaction forces and displacements are captured at each increment in the displacement directions (Fig. 17a–c).

In a similar way, the stress–strain curves under biaxial tensile x–y loading conditions are constructed by displacing the edge nodes by a specified amount, while the nodes at the opposite edge are prevented from translating in the direction of the displacement. The displacements are imposed at the both sides, which means that boundary conditions are imposed at all four sides (x and y directions). The stress–stretch responses are then constructed from the reaction forces and displacements, both captured at each increment in the displacement directions (x and y). The effective uniaxial stresses in x and y directions computed from FE simulations compare well with those obtained by discrete homogenization, as shown in Fig. 18.

A FE simulation for simple shear in x–y plane is additionally performed to deliver the shear response for each displacement loading step. In this simulation, we impose a displacement field on the top surface of the unit cell along the x direction, while the bottom surface is constrained in the same direction. Both the left and right surfaces are also prevented from translating in the direction perpendicular to x. The shear stress–strain response is then constructed from the reaction force and displacement at each increment. The evolutions of the effective shear stress obtained from the DH method and FE simulations show a quite good agreement (Fig. 19).

A relatively good agreement is obtained between the stress–strain responses predicted by finite elements and those calculated by discrete homogenization, which shows that the developed discrete homogenization method has the ability to deliver the effective response of these structures in the nonlinear regime with a good accuracy and at a low numerical cost.

The displacement distributions over the 3D hexagonal unit cell under uniaxial tension in x, y and z, biaxial tension in x–y plane and in-plane shear are pictured on Fig. 20.

4.2 FE validation of the nonlinear responses of plain weave and twill

In the current section, 3D finite element models of woven fabrics at meso-level are developed to evaluate the accuracy of the effective mechanical properties predicted from discrete homogenization. The FE model is capable of simulating elementary cells under simultaneous axial loadings along both yarn directions. The previous results for the stress–strain response obtained with the DH technique are now compared with numerical results obtained from the FE method (ABAQUS), under the specified types of loadings (we restrict the validation of the computed response to uniaxial and biaxial tests), with appropriate boundary conditions. The warp and weft yarns are meshed with the eight-node solid linear hexahedral element (ABAQUS element type C3D8); a total of 14,804 elements are used to model the balanced plain weave. In order to account for the

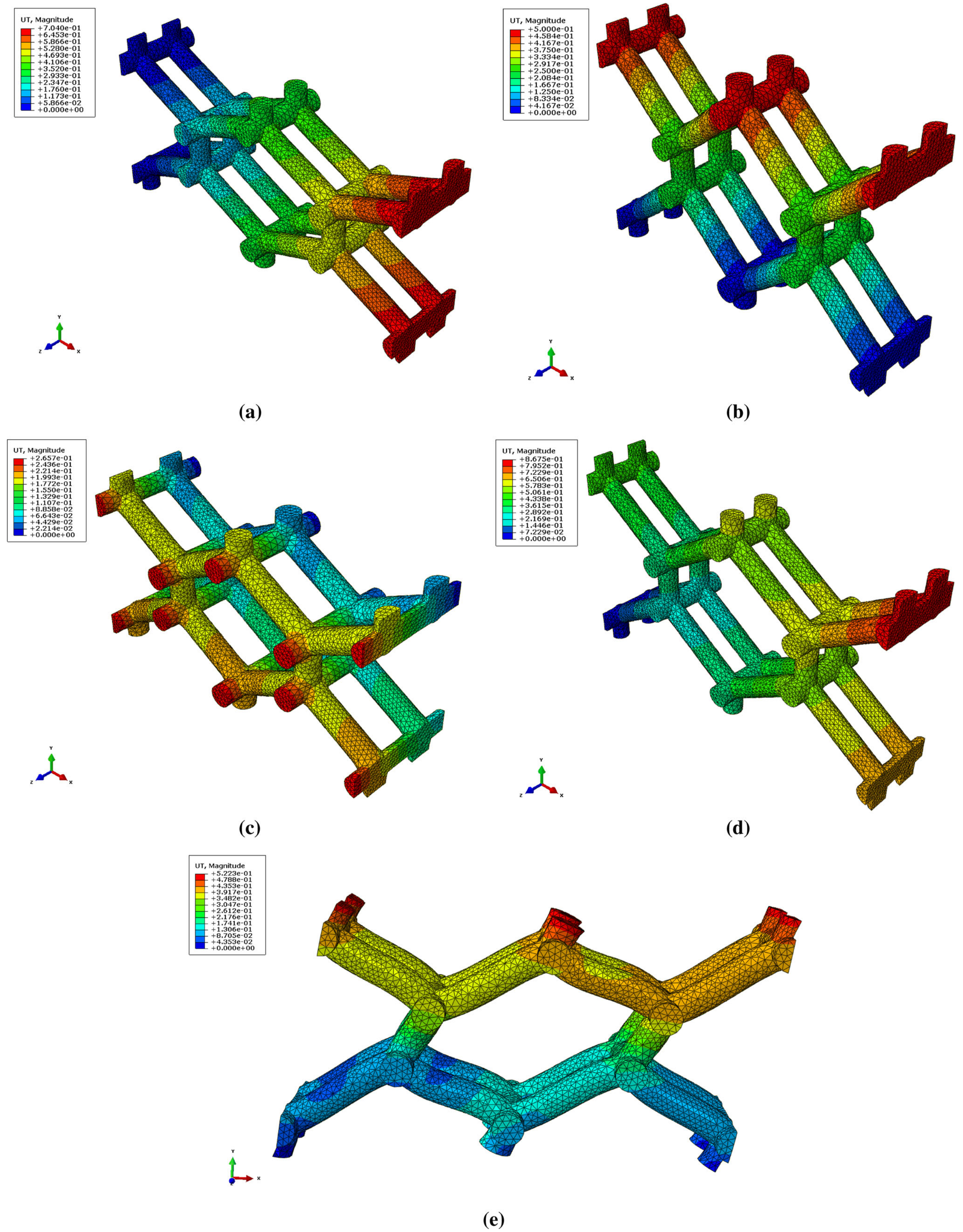

(a) **(b)** **(c)** **(d)** **(e)**

Fig. 20 Displacement distributions over the 3D hexagonal unit cell submitted to a uniaxial test in **a** x-direction, **b** y-direction, **c** z-direction, **d** equi-biaxial test in x–y plane and **e** in-plane shear test

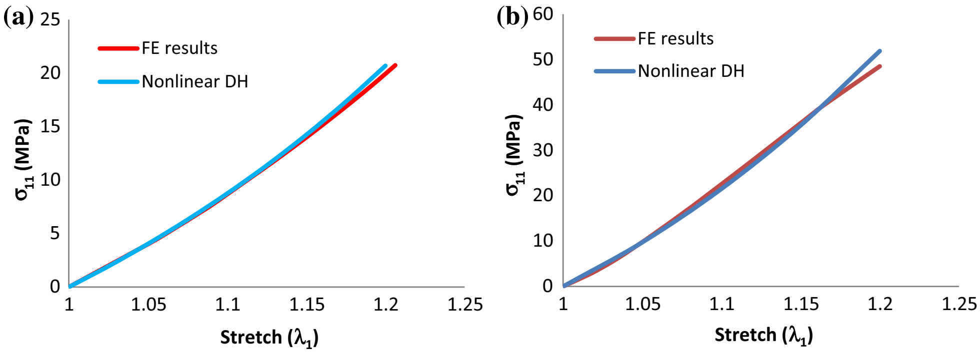

Fig. 21 Comparison of the uniaxial tensile response for **a** balanced plain weave and **b** twill between the DH method and FE simulations

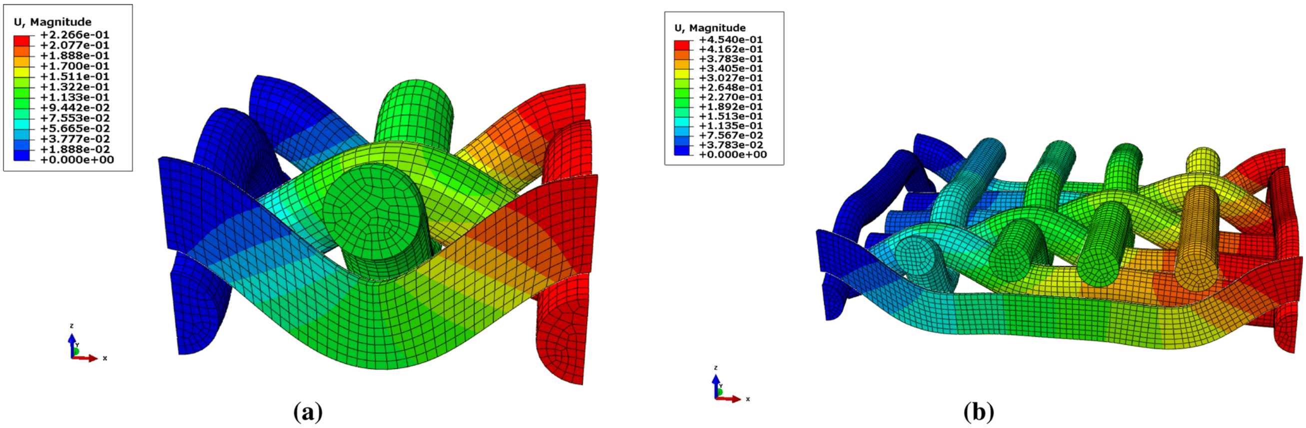

Fig. 22 Displacement distributions over **a** balanced plain weave and **b** twill submitted to a uniaxial test in x- direction

possible relative displacements between the yarns, a contact with friction is introduced with a master/slave approach. Contact is considered to be an intrinsic character of woven fabrics which cannot be neglected during the meso-level analysis. Contact conditions are prescribed between the possible interlacing surfaces of the yarns under loading and are the same for all loading cases. The tangential behavior at the contact surfaces in the frame of Coulomb friction model is defined using the penalty method with a friction coefficient selected here as 0.05, relying on data from [35].

The uniaxial response for the balanced plain weave is shown in Fig. 21 (left); a good agreement is obtained using both methods (DH and FE simulations), with a maximum discrepancy close to 1.41 % in the uniaxial test for the considered unit cell of plain weave (Fig. 21, left), and close to 6 % at 20 % for twill submitted to uniaxial strain (Fig. 21, right).

The displacement distribution over the RUC under uniaxial test conditions for both plain weave and twill patterns are pictured on Fig. 22.

4.3 Validation of he homogenized response of 3D textile structure

We validate the stress–strain responses obtained with the DH method with full FE computations performed under the specified types of loadings (uniaxial and equibiaxial) applied on the representative unit cell (see Fig. 23).

The displacement distributions over the RUC for the 2.5D layer-to-layer under both uniaxial and biaxial testing conditions are pictured in Fig. 24.

The discrepancy (about 15 % at 20 % strain) observed between the response computed by DH and FE simulations is possibly due to the choice of the contact beam rigidities; accordingly, we next conduct a sensitivity analysis to evaluate the effect of the contact beam rigidities (tensile, flexural and torsional rigidities) on the global behavior of the 2.5D layer-to-layer angle interlock.

The range of variation of the contact beam rigidity has been chosen as 0.1–10 times the longitudinal beam rigidity. The evolutions of the x component of the Cauchy stress versus stretch obtained with the DH technique are compared

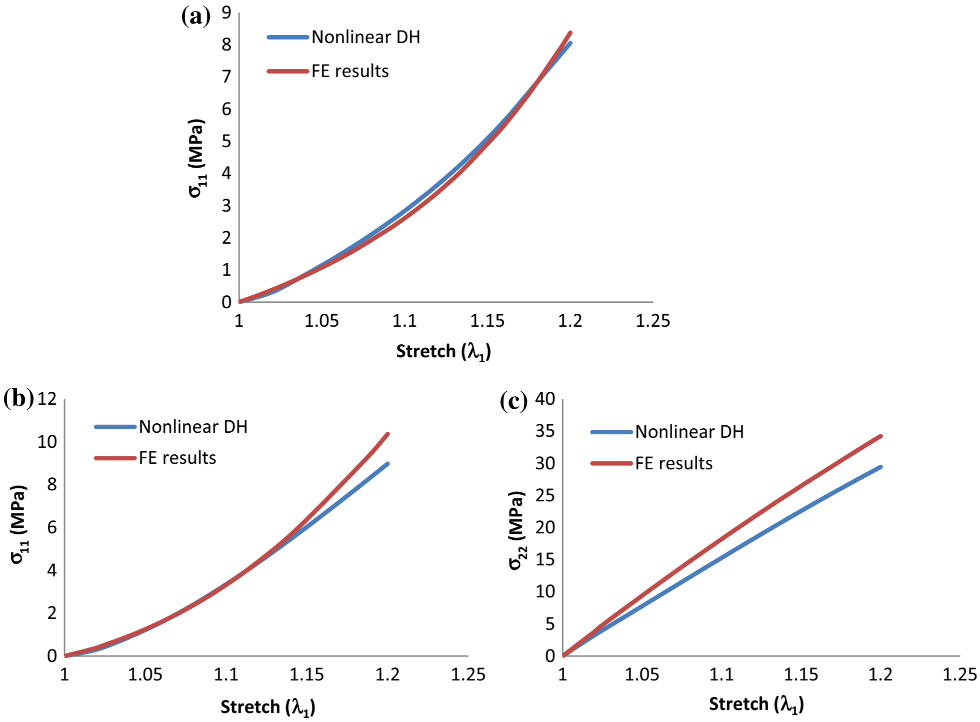

Fig. 23 **a** Comparison of the uniaxial tensile response and **b, c** the equibiaxial tensile response for the 2.5D layer-to-layer interlock between the DH method and FE simulations

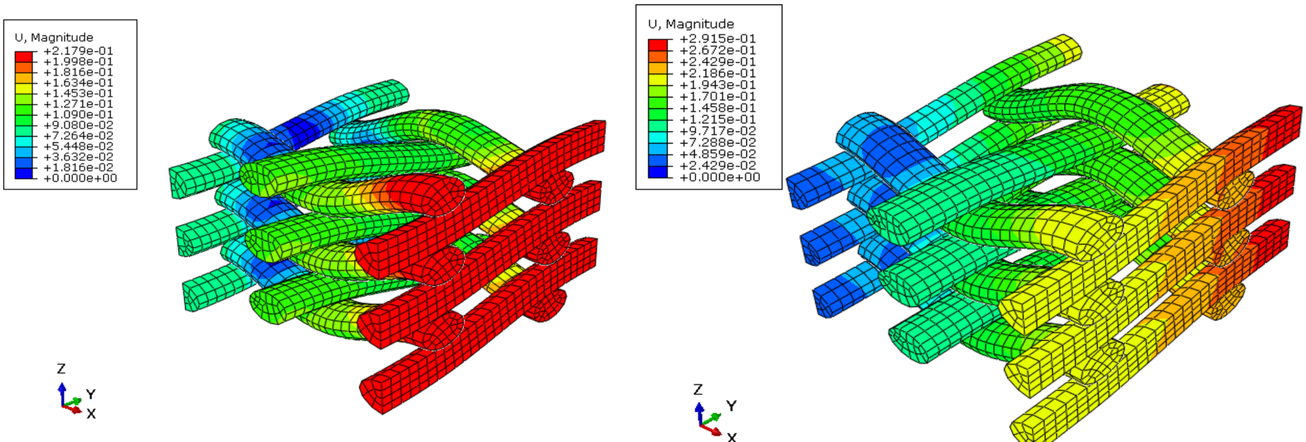

(a) (b)

Fig. 24 Displacement distributions over the 2.5D layer to layer interlock due to **a** uniaxial extension in x direction and **b** equi-biaxial extension in xy direction

with FE results (ABAQUS), under an equibiaxial loading, for four values of the flexural rigidity of the contact beams.

Independent computations show that the tensile and torsion rigidities of the contact beams have relatively small (almost zero) effect on the nonlinear response. In contrast to this, a variation of the flexural rigidity has a significant effect, with the percentage of difference variation between DH and FE results from 13.31 to 2.89 % for the Cauchy stress in x-direction and from 14 to 9.52 % for the stress in y-direction, as shown in Fig. 25. The mechanical properties of the contact beams are unknown in the absence of measurements, so that they are adjusted by an inverse approach based on a comparison of the response of the DH method with full scale FE computations over the RUC. The conclusion of the adjustment is that the transverse rigidity of the yarn represented by the contact beam elements is not the only factor to be considered, since also inter-yarn friction is expected to play an important role, as explained in [1].

A few words about the computational cost of the employed DH method in comparison to FE computations are in order. In

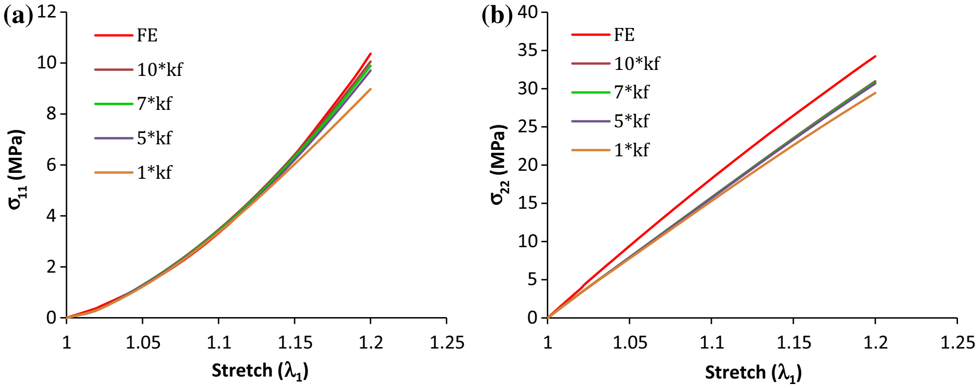

Fig. 25 Effect of flexural rigidity of the contact beam on the stress–strain response from nonlinear discrete homogenization compared with FE simulations

fact a high accuracy of local stress peak requires fine meshes resulting in long computation times. In addition, large deformation problems can result in a huge number of degrees of freedom effectively increasing the size of stiffness matrices. Larger the stiffness matrix longer is the computational time required. In comparison, the DH method involves comparatively a much small number of degrees of freedom since the beam degrees of freedom within the unit cell are only defined at its extremity nodes.

Considering next to be specific the 2.5D layer to layer interlock, the computational time is much reduced with the DH method (few minutes on a two-core processor machine) in comparison to FE computations (1 hr on the same machine), due to the strong reduction of the number of degrees of freedom.

From a numerical viewpoint, the developed DH algorithms can be easily implemented as they rely on a text file including all necessary input data (geometry of the structure and microscopic properties of the beams in terms of their geometry and mechanical properties). The low cost computations allow computing in a quite efficient manner the effective anisotropic mechanical properties of 3D repetitive network materials.

5 Summary and future work

The development of suitable micromechanical schemes for the computation of the effective mechanical response of architecture materials such as fibrous networks is quite important, in order to have at hand predictive models to analyze the overall computed response in terms of the underlying microscopic mechanisms. When a RUC can be identified for a quasi periodic network, it is possible to develop specific homogenization schemes relying on the assumption of inherent periodicity. Although a lot of attention has been devoted to replacing large periodic networks of lattice materials by effective continuum models, less attention has been paid to the consideration of both geometrical nonlinearities and microstructure effects leading to generalized continua at the continuum level.

We presently extended the linear discrete asymptotic homogenization framework to the nonlinear setting, based on an update of the lattice geometry and elastic computations done incrementally under a kinematic control. A novel procedure for predicting the effective nonlinear elastic responses of these repetitive lattices through a combined linear and nonlinear discrete homogenization scheme has been presented. The nonlinear stress–strain and couple stress–curvature responses have been analyzed incrementally for different 3D structures under different loading cases: uniaxial, biaxial, simple shear, and bending, taking into consideration changes of the structure geometry. The combination of the incremental scheme with the homogenization method delivers both the classical and nonclassical properties; especially, the micropolar framework allows deriving the bending response.

These theoretical developments have been implemented into a dedicated code using the lattice geometry and microstructural properties as an input, and delivering as an output the effective response in the nonlinear range at the mesoscopic continuum level of the RUC.

These nonlinear homogenization schemes have been applied to meso-level analyses of the mechanical behavior of textile monolayers, 2.5D layer-to-layer interlocks and 3D hexagonal lattices to construct their effective anisotropic micropolar continuum response at the mesoscopic level.

The chief advantage of the discrete homogenization technique developed in the present work is inherent to its predictive and systematic nature, and its numerical efficiency in comparison to FE methods.

The proposed micromechanical approach is particularly appealing, due to the difficulty to measure such effective properties for textiles considering their discreteness. The proposed homogenization technique proves efficient from a numerical point of view, and it has a great versatility as to the topology of the textile armor, which makes it a suitable tool to explore and compare in future developments various textile architectures for both single and multilayer 3D configurations. More generally speaking, the potentiality and versatility of the method shall enable to compute the mechanical response of architectured materials having a repetitive microstructure.

Appendix 1: Small strains homogenization: expressions of forces, moments and virtual translation and rotation velocities

The first order normal and transverse forces and the second order moment about x′, y′, and z′ at the beam extremities can be successively expressed versus the kinematical nodal variables as

$$F_x^{\varepsilon b} = \frac{E_s^b A^{\varepsilon b}}{l^{\varepsilon b}} \left(\mathbf{e}_x \cdot \left(\varepsilon \Delta \mathbf{U}_1^{\mathrm{b}} + \varepsilon^2 \Delta \mathbf{U}_2^{\mathrm{b}}\right)\right) \tag{29}$$

$$\begin{aligned} F_y^{\varepsilon b} = {} & \frac{12 E_s^b I_z^{\varepsilon b}}{\left(l^{\varepsilon b}\right)^3} \bigg(\mathbf{e}_y \cdot \left(\varepsilon \Delta \mathbf{U}_1^{\mathrm{b}} + \varepsilon^2 \Delta \mathbf{U}_2^{\mathrm{b}}\right) \\ & - \frac{l^{\varepsilon b}}{2} \bigg(\mathbf{e}_z \cdot \bigg(\boldsymbol{\varphi}_0^{O_{R(b)}} + \boldsymbol{\varphi}_0^{E_{R(b)}} + \varepsilon \bigg(\boldsymbol{\varphi}_1^{O_{R(b)}} + \boldsymbol{\varphi}_1^{E_{R(b)}} \\ & + \frac{\partial \boldsymbol{\varphi}_0}{\partial \beta^i} \delta^{ib}\bigg)\bigg)\bigg)\bigg) \end{aligned} \tag{30}$$

$$\begin{aligned} F_z^{\varepsilon b} = {} & \frac{12 E_s^b I_y^{\varepsilon b}}{\left(l^{\varepsilon b}\right)^3} \bigg(\mathbf{e}_z \cdot \left(\varepsilon \Delta \mathbf{U}_1^{\mathrm{b}} + \varepsilon^2 \Delta \mathbf{U}_2^{\mathrm{b}}\right) \\ & + \frac{l^{\varepsilon b}}{2} \bigg(\mathbf{e}_y \cdot \bigg(\boldsymbol{\varphi}_0^{O_{R(b)}} + \boldsymbol{\varphi}_0^{E_{R(b)}} + \varepsilon \bigg(\boldsymbol{\varphi}_1^{O_{R(b)}} + \boldsymbol{\varphi}_1^{E_{R(b)}} \\ & + \frac{\partial \boldsymbol{\varphi}_0}{\partial \beta^i} \delta^{ib}\bigg)\bigg)\bigg)\bigg) \end{aligned} \tag{31}$$

$$\begin{aligned} M_x^{O(b)\varepsilon} &= \frac{G_s^b J^{\varepsilon b}}{l^{\varepsilon b}} \varepsilon \left(\mathbf{e}_x \cdot \left(\boldsymbol{\varphi}_1^{O_{R(b)}} - \left(\frac{\partial \boldsymbol{\varphi}_0}{\partial \beta^i} \delta^{ib} + \boldsymbol{\varphi}_1^{E_{R(b)}}\right)\right)\right) \\ M_x^{E(b)\varepsilon} &= \frac{G_s^b J^{\varepsilon b}}{l^{\varepsilon b}} \varepsilon \left(\mathbf{e}_x \cdot \left(\boldsymbol{\varphi}_1^{E_{R(b)}} - \boldsymbol{\varphi}_1^{O_{R(b)}} + \frac{\partial \boldsymbol{\varphi}_0}{\partial \beta^i} \delta^{ib}\right)\right) \end{aligned} \tag{32}$$

$$\begin{aligned} M_y^{O(b)\varepsilon} = {} & \frac{6 E_s^b I_y^{\varepsilon b}}{\left(l^{\varepsilon b}\right)^2} \left(\mathbf{e}_z \cdot \left(\varepsilon \Delta \mathbf{U}_1^{\mathrm{b}} + \varepsilon^2 \Delta \mathbf{U}_2^{\mathrm{b}}\right)\right) \\ & + \frac{E_s^b I_y^{\varepsilon b}}{l^{\varepsilon b}} \bigg(\mathbf{e}_y \cdot \bigg(4\boldsymbol{\varphi}_0^{O_{R(b)}} + 2\boldsymbol{\varphi}_0^{E_{R(b)}} + \varepsilon \bigg(4\boldsymbol{\varphi}_1^{O_{R(b)}} \\ & + 2\boldsymbol{\varphi}_1^{E_{R(b)}} + 2 \frac{\partial \boldsymbol{\varphi}_0}{\partial \beta^i} \delta^{ib}\bigg)\bigg)\bigg) \\ M_y^{E(b)\varepsilon} = {} & \frac{6 E_s^b I_y^{\varepsilon b}}{\left(l^{\varepsilon b}\right)^2} \left(\mathbf{e}_z \cdot \left(\varepsilon \Delta \mathbf{U}_1^{\mathrm{b}} + \varepsilon^2 \Delta \mathbf{U}_2^{\mathrm{b}}\right)\right) \\ & + \frac{E_s^b I_y^{\varepsilon b}}{l^{\varepsilon b}} \bigg(\mathbf{e}_y \cdot \bigg(2\boldsymbol{\varphi}_0^{O_{R(b)}} + 4\boldsymbol{\varphi}_0^{E_{R(b)}} + \varepsilon \bigg(2\boldsymbol{\varphi}_1^{O_{R(b)}} \\ & + 4\boldsymbol{\varphi}_1^{E_{R(b)}} + 4 \frac{\partial \boldsymbol{\varphi}_0}{\partial \beta^i} \delta^{ib}\bigg)\bigg)\bigg) \end{aligned} \tag{33}$$

$$\begin{aligned} M_z^{O(b)\varepsilon} = {} & \frac{6 E_s^b I_z^{\varepsilon b}}{\left(l^{\varepsilon b}\right)^2} \left(-\mathbf{e}_y \cdot \left(\varepsilon \Delta \mathbf{U}_1^{\mathrm{b}} + \varepsilon^2 \Delta \mathbf{U}_2^{\mathrm{b}}\right)\right) \\ & + \frac{E_s^b I_z^{\varepsilon b}}{l^{\varepsilon b}} \bigg(\mathbf{e}_z \cdot \bigg(4\boldsymbol{\varphi}_0^{O_{R(b)}} + 2\boldsymbol{\varphi}_0^{E_{R(b)}} + \varepsilon \bigg(4\boldsymbol{\varphi}_1^{O_{R(b)}} \\ & + 2\boldsymbol{\varphi}_1^{E_{R(b)}} + 2 \frac{\partial \boldsymbol{\varphi}_0}{\partial \beta^i} \delta^{ib}\bigg)\bigg)\bigg) \\ M_z^{E(b)\varepsilon} = {} & \frac{6 E_s^b I_z^{\varepsilon b}}{\left(l^{\varepsilon b}\right)^2} \left(-\mathbf{e}_y \cdot \left(\varepsilon \Delta \mathbf{U}_1^{\mathrm{b}} + \varepsilon^2 \Delta \mathbf{U}_2^{\mathrm{b}}\right)\right) \\ & + \frac{E_s^b I_z^{\varepsilon b}}{l^{\varepsilon b}} \bigg(\mathbf{e}_z \cdot \bigg(2\boldsymbol{\varphi}_0^{O_{R(b)}} + 4\boldsymbol{\varphi}_0^{E_{R(b)}} + \varepsilon \\ & \times \bigg(2\boldsymbol{\varphi}_1^{O_{R(b)}} + 4\boldsymbol{\varphi}_1^{E_{R(b)}} + 4 \frac{\partial \boldsymbol{\varphi}_0}{\partial \beta^i} \delta^{ib}\bigg)\bigg)\bigg) \end{aligned} \tag{34}$$

where E_s^b and G_s^b the tensile and shear modulus of the bulk material.

The asymptotic development of the virtual velocity and rotation rate are next expressed. For any virtual velocity field $\mathbf{v}^{\varepsilon}(\beta)$, a Taylor series expansion leads to

$$\mathbf{v}^{\varepsilon}(\mathrm{O}(\mathrm{b})) - \mathbf{v}^{\varepsilon}(\mathrm{E}(\mathrm{b})) \approx \varepsilon \frac{\partial \mathbf{v}\left(\beta^{\varepsilon}\right)}{\partial \beta^{\mathrm{i}}} \delta^{\mathrm{ib}} \tag{35}$$

The rotation rate field is similarly expanded taking into account the central node of the beam, so that a change of curvature of any beam can be captured:

$$\begin{aligned} \mathbf{w}^{\mathrm{O(b)}\,\varepsilon}(\beta) = \mathbf{w}(\beta); \quad & \mathbf{w}^{\mathrm{E(b)}\,\varepsilon}\left(\beta + \varepsilon\, \delta^{\mathrm{i}}\right) = \mathbf{w}(\beta) \\ & + \varepsilon \frac{\partial \mathbf{w}(\beta)}{\partial \beta^{\mathrm{i}}} \delta^{\mathrm{i}} \end{aligned} \tag{36}$$

Appendix 2: Computation of the tangent stiffness matrix for the DH scheme

The variations of the beam orientation and length are obtained after straightforward computations as follows:

$$\begin{aligned} & \delta\, \mathbf{e}_{\mathrm{x}}^{\mathrm{b}} = \mathbf{C} \cdot \mathbf{P} \cdot \delta\, \mathbf{B}^{\mathrm{b}} / \mathrm{l}^{\mathrm{b}},\ \delta\, \mathbf{e}_{\mathrm{y}}^{\mathrm{b}} = \boldsymbol{\Omega}_{\mathrm{z}} \cdot \delta\, \mathbf{e}_{\mathrm{x}}^{\mathrm{b}},\ \delta\, \mathbf{e}_{\mathrm{z}}^{\mathrm{b}} = \boldsymbol{\Omega}_{\mathrm{y}} \cdot \delta\, \mathbf{e}_{\mathrm{x}}^{\mathrm{b}} \\ & \delta\, \mathrm{l}^{\mathrm{b}} = \mathbf{B}^{\mathrm{b}} \cdot [\mathbf{I} + \mathbf{C} \cdot \mathbf{P}] \cdot \delta\, \mathbf{B}^{\mathrm{b}} / \mathrm{l}^{\mathrm{b}} \end{aligned} \tag{37}$$

In (37), we have introduced the projection operators **P** and **C** expressing as

$$\mathbf{P} = \left(\mathbf{I} - \mathbf{e}_x^b \otimes \mathbf{e}_x^b\right), \quad \mathbf{C} = \left(\mathbf{I} - \frac{1}{2}\mathbf{e}_x^b \otimes \mathbf{e}_x^b\right) \tag{38}$$

In the present large strains regime, since the beam length is changing, one has to expand it versus the asymptotic parameter ε as for all other kinematic variables (these expansions are not repeated in this subsection),

$$l^b = l_0^b + \varepsilon\, l_1^b + \varepsilon^2 l_2^b + \cdots + \varepsilon^p l_p^b \tag{39}$$

The induced perturbations of the forces and moments are then obtained as

$$\begin{aligned}
\delta F_X^{b(k)} \mathbf{e}_X^b &= \frac{1}{l^b}\frac{dF_X^{b(k)}}{dl^b}\left(\mathbf{B}^b \otimes \mathbf{B}^b\left[\mathbf{I} + \mathbf{C}\cdot\mathbf{P}\right]\right)\cdot\delta\,\mathbf{B}^b\\
\delta F_y^{b(k)} \mathbf{e}_y^b &= \frac{1}{l^b}\frac{dF_y^{b(k)}}{dl^b}\left(\mathbf{e}_y^b \otimes \mathbf{B}^b\left[\mathbf{I} + \mathbf{C}\cdot\mathbf{P}\right]\right)\cdot\delta\,\mathbf{B}^b\\
&\quad+\left(\frac{-6E_s^b I_z}{\left(l^b\right)^2}\right)\left[\left(\mathbf{e}_y^b \otimes \mathbf{e}_z^b\right)\cdot\delta\,\boldsymbol{\varphi}^{O(b)} + \left(\mathbf{e}_y^b \otimes \mathbf{e}_z^b\right)\cdot\delta\,\boldsymbol{\varphi}^{E(b)}\right]\\
\delta F_z^{b(k)} \mathbf{e}_z^b &= \frac{1}{l^b}\frac{dF_z^{b(k)}}{dl^b}\left(\mathbf{e}_z^b \otimes \mathbf{B}^b\left[\mathbf{I} + \mathbf{C}\cdot\mathbf{P}\right]\right)\cdot\delta\,\mathbf{B}^b\\
&\quad+\left(\frac{6E_s^b I_y}{\left(l^b\right)^2}\right)\left[\left(\mathbf{e}_z^b \otimes \mathbf{e}_y^b\right)\cdot\delta\,\boldsymbol{\varphi}^{O(b)} + \left(\mathbf{e}_z^b \otimes \mathbf{e}_y^b\right)\cdot\delta\,\boldsymbol{\varphi}^{E(b)}\right]\\
\\
\delta M_X^O \mathbf{e}_X^b &= \left(\frac{G_s^b J^b}{l^b}\right)\left[\left(\mathbf{e}_X^b \otimes \mathbf{e}_X^b\right)\cdot\delta\,\boldsymbol{\varphi}^{O(b)} - \left(\mathbf{e}_X^b \otimes \mathbf{e}_X^b\right)\cdot\delta\,\boldsymbol{\varphi}^{E(b)}\right]\\
\delta M_X^E \mathbf{e}_X^b &= \left(\frac{G_s^b J^b}{l^b}\right)\left[\left(\mathbf{e}_X^b \otimes \mathbf{e}_X^b\right)\cdot\delta\,\boldsymbol{\varphi}^{E(b)} - \left(\mathbf{e}_X^b \otimes \mathbf{e}_X^b\right)\cdot\delta\,\boldsymbol{\varphi}^{O(b)}\right]\\
\delta M_y^O \mathbf{e}_y^b &= \frac{dM_y^O}{dl^b}\left(\mathbf{B}^b \otimes \mathbf{B}^b\left[\mathbf{I} + \mathbf{C}\cdot\mathbf{P}\right]\right)\cdot\boldsymbol{\Omega}_z\cdot\delta\,\mathbf{B}^b\\
&\quad+\left(\frac{E_s^b I_y^b}{l^b}\right)\left[4\left(\mathbf{e}_y^b \otimes \mathbf{e}_y^b\right)\cdot\delta\,\boldsymbol{\varphi}^{O(b)} - 2\left(\mathbf{e}_y^b \otimes \mathbf{e}_y^b\right)\cdot\delta\,\boldsymbol{\varphi}^{E(b)}\right]\\
\delta M_y^E \mathbf{e}_y^b &= \frac{dM_y^E}{dl^b}\left(\mathbf{B}^b \otimes \mathbf{B}^b\left[\mathbf{I} + \mathbf{C}\cdot\mathbf{P}\right]\right)\cdot\boldsymbol{\Omega}_z\cdot\delta\,\mathbf{B}^b\\
&\quad+\left(\frac{E_s^b I_y^b}{l^b}\right)\left[2\left(\mathbf{e}_y^b \otimes \mathbf{e}_y^b\right)\cdot\delta\,\boldsymbol{\varphi}^{E(b)} - 4\left(\mathbf{e}_y^b \otimes \mathbf{e}_y^b\right)\cdot\delta\,\boldsymbol{\varphi}^{O(b)}\right]\\
\delta M_z^O \mathbf{e}_z^b &= \frac{dM_z^O}{dl^b}\left(\mathbf{B}^b \otimes \mathbf{B}^b\left[\mathbf{I} + \mathbf{C}\cdot\mathbf{P}\right]\right)\cdot\boldsymbol{\Omega}_y\cdot\delta\,\mathbf{B}^b\\
&\quad+\left(\frac{E_s^b I_z^b}{l^b}\right)\left[4\left(\mathbf{e}_z^b \otimes \mathbf{e}_z^b\right)\cdot\delta\,\boldsymbol{\varphi}^{O(b)} - 2\left(\mathbf{e}_z^b \otimes \mathbf{e}_z^b\right)\cdot\delta\,\boldsymbol{\varphi}^{E(b)}\right]\\
\delta M_z^E \mathbf{e}_z^b &= \frac{dM_z^E}{dl^b}\left(\mathbf{B}^b \otimes \mathbf{B}^b\left[\mathbf{I} + \mathbf{C}\cdot\mathbf{P}\right]\right)\cdot\boldsymbol{\Omega}_y\cdot\delta\,\mathbf{B}^b\\
&\quad+\left(\frac{E_s^b I_z^b}{l^b}\right)\left[2\left(\mathbf{e}_z^b \otimes \mathbf{e}_z^b\right)\cdot\delta\,\boldsymbol{\varphi}^{E(b)} - 4\left(\mathbf{e}_z^b \otimes \mathbf{e}_z^b\right)\cdot\delta\,\boldsymbol{\varphi}^{O(b)}\right]
\end{aligned} \tag{40}$$

We introduced in (40) the two orthogonal transformations $\boldsymbol{\Omega}_y$, $\boldsymbol{\Omega}_z$ elaborated as

$$\begin{aligned}
\boldsymbol{\Omega}_y\left(\mathbf{e}_x^b, \mathbf{e}_z^b, y\right) &= \begin{bmatrix} \cos\left(\frac{\pi}{2}\right) & 0 \ \sin\left(\frac{\pi}{2}\right) \\ 0 & 1 \ 0 \\ -\sin\left(\frac{\pi}{2}\right) & 0 \ \cos\left(\frac{\pi}{2}\right) \end{bmatrix}\\
\boldsymbol{\Omega}_z\left(\mathbf{e}_x^b, \mathbf{e}_y^b, z\right) &= \begin{bmatrix} \cos\left(\frac{\pi}{2}\right) & -\sin\left(\frac{\pi}{2}\right) & 0 \\ \sin\left(\frac{\pi}{2}\right) & \cos\left(\frac{\pi}{2}\right) & 0 \\ 0 & 0 & 1 \end{bmatrix}
\end{aligned} \tag{41}$$

The linear stiffness, the initial displacement stiffness and initial stress stiffness express successively as

$$\begin{aligned}
\mathbf{K}_{So}^b &= \frac{E_S^b A^b}{l^b}\left(\mathbf{e}_x^b \otimes \mathbf{e}_x^b\right) + \left(\frac{12E_S^b I_y^b}{\left(l^b\right)^3}\right)\left(\mathbf{e}_y^b \otimes \mathbf{e}_y^b\right)\\
&\quad+\left(\frac{12E_S^b I_z^b}{\left(l^b\right)^3}\right)\left(\mathbf{e}_z^b \otimes \mathbf{e}_z^b\right)
\end{aligned} \tag{42}$$

$$\begin{aligned}
\mathbf{K}_u^b &= \frac{E_S^b A^b}{L}\left[\left(\frac{1}{l^b}\right)\left(\mathbf{e}_x^b \otimes \left(\mathbf{B}^b - \mathbf{B}_o^b\right)\right)\cdot\left(\mathbf{C}.\mathbf{P}\right)\right.\\
&\quad\left.-\frac{\left(\mathbf{B}^b - \mathbf{B}_o^b\right)\cdot\mathbf{e}_x^b}{\left(l^b\right)^2}\left(\left(\mathbf{e}_x^b \otimes \mathbf{B}^b\right)\cdot\left[I + \mathbf{C}.\mathbf{P}\right]\right)\right]\\
&\quad+\left(\frac{12E_S^b I_y^b}{\left(l^b\right)^3}\right)\left[\left(\left(\frac{1}{l^b}\right)\left(\mathbf{e}_y^b \otimes \left(\mathbf{B}^b - \mathbf{B}_o^b\right)\right)\cdot\left(\boldsymbol{\Omega}_z\cdot\mathbf{C}.\mathbf{P}\right)\right.\right.\\
&\quad\left.\left.-\frac{\left(\mathbf{B} - \mathbf{B}_o^b\right)\cdot\mathbf{e}_y^b}{\left(l^b\right)^2}\left(\left(\mathbf{e}_y^b \otimes \mathbf{B}^b\right)\cdot\left[I + \mathbf{C}.\mathbf{P}\right]\right)\right)\right]\\
&\quad+\left(\frac{12E_S^b I_z^b}{\left(l^b\right)^3}\right)\left[\left(\begin{array}{l}\left(\frac{1}{l^b}\right)\left(\mathbf{e}_z^b \otimes \left(\mathbf{B}^b - \mathbf{B}_o^b\right)\right)\cdot\left(\boldsymbol{\Omega}_y\cdot\mathbf{C}.\mathbf{P}\right) - \\ \frac{\left(\mathbf{B}-\mathbf{B}_o^b\right)\cdot\mathbf{e}_z^b}{\left(l^b\right)^2}\left(\left(\mathbf{e}_z^b \otimes \mathbf{B}^b\right)\cdot\left[I + \mathbf{C}.\mathbf{P}\right]\right)\end{array}\right)\right]
\end{aligned} \tag{43}$$

$$\begin{aligned}
\mathbf{K}_\sigma^b &= \left[\left(\frac{F_x^b}{l^b}\right)\mathbf{C}.\mathbf{P}\right] + \left[\left(\frac{2F_y^b}{\left(l^b\right)^2}\right)\left(\left(\mathbf{e}_y^b \otimes \mathbf{B}^b\right)\cdot\left[I + \mathbf{C}.\mathbf{P}\right]\right)\right]\\
&\quad+\left[\left(\frac{2F_z^b}{\left(l^b\right)^2}\right)\left(\left(\mathbf{e}_z^b \otimes \mathbf{B}^b\right)\cdot\left[I + \mathbf{C}.\mathbf{P}\right]\right)\right]\\
&\quad+\left[\left(\frac{F_y^b}{l^b}\right)\left(\boldsymbol{\Omega}_z\cdot\mathbf{C}.\mathbf{P}\right)\right] + \left[\left(\frac{F_z^b}{l^b}\right)\left(\boldsymbol{\Omega}_y\cdot\mathbf{C}.\mathbf{P}\right)\right]
\end{aligned} \tag{44}$$

The tangent couple stress stiffness matrix therein express as

$$\begin{aligned}
\mathbf{K}_{mo}^b &= \left(\frac{-6E_s^b I_y^b}{\left(l^b\right)^2}\right)\left(\mathbf{e}_y^b \otimes \mathbf{e}_z^b\right) + \left(\frac{-6E_s^b I_z^b}{\left(l^b\right)^2}\right)\left(\mathbf{e}_z^b \otimes \mathbf{e}_y^b\right)\\
&\quad+\left(\frac{E_s^b J^b}{l^b}\right)\left(\mathbf{e}_x^b \otimes \mathbf{e}_x^b\right) + \left(\frac{E_s^b I_y^b}{l^b}\right)\left(\mathbf{e}_y^b \otimes \mathbf{e}_y^b\right)\\
&\quad+\left(\frac{E_s^b I_z^b}{l^b}\right)\left(\mathbf{e}_z^b \otimes \mathbf{e}_z^b\right)
\end{aligned} \tag{45}$$

$$\mathbf{K}_m^b = \left[\left(\frac{M_x^{E(b)}}{l^b}\right)\mathbf{C}\cdot\mathbf{P} + \left(\frac{M_x^{O(b)}}{l^b}\right)\mathbf{C}\cdot\mathbf{P}\right]$$

$$+\left[\left(\frac{\mathrm{M}_{\mathrm{y}}^{\mathrm{E(b)}}}{\mathrm{l}^{\mathrm{b}}}\right)\boldsymbol{\Omega}_{\mathrm{z}}\cdot\mathbf{C}\cdot\mathbf{P}+\left(\frac{\mathrm{M}_{\mathrm{y}}^{\mathrm{O(b)}}}{\mathrm{l}^{\mathrm{b}}}\right)\boldsymbol{\Omega}_{\mathrm{z}}\cdot\mathbf{C}\cdot\mathbf{P}\right]$$
$$+\left[\left(\frac{\mathrm{M}_{\mathrm{z}}^{\mathrm{E(b)}}}{\mathrm{l}^{\mathrm{b}}}\right)\boldsymbol{\Omega}_{\mathrm{y}}\cdot\mathbf{C}\cdot\mathbf{P}+\left(\frac{\mathrm{M}_{\mathrm{z}}^{\mathrm{O(b)}}}{\mathrm{l}^{\mathrm{b}}}\right)\boldsymbol{\Omega}_{\mathrm{y}}\cdot\mathbf{C}\cdot\mathbf{P}\right] \quad (46)$$

Appendix 3: Geometrical and mechanical parameters for the considered textile performs

The geometrical parameters for plain weave and twill are given in Table 3.

Mechanical properties of weft and warp made of PET are given in Table 4; we intentionally choose very different moduli to represent an unbalanced fabric, leading to an expected anisotropic behavior.

The mechanical properties of the yarns are the same for both unit cells. The tensile, flexural, and torsion rigidities of the beam segments are given in Table 5.

Furthermore, the geometric and material parameters for the contact beam are

$$L_{c_{1,2}} = Lf_1 Sin\theta_f,\, Lp_1 Sin\theta_p,\, r_c = \frac{r_f + r_p}{2},\, G_{sc} = \frac{G_{sf}+G_{pf}}{2},\ \text{and } E_{sc} = \frac{E_{sf}+E_{pf}}{2}$$

where $L_{c1,2}$, r_c, G_{sc}, and E_{sc}, represent the lengths, radius, shear and Young's modulus of the contact beams respectively (beams connecting the warp and weft yarns at their crossing points). As an assumption, we take the contact beam with radius and mechanical modulus as average values from the weft and warp corresponding values.

Table 3 Plain weave and twill fabric configuration parameter

Weave	Set of input geometric data required for modeling			
Plain				
Weft	$L_{f1} = 0.618$ mm	–	$\theta_f = 40°$	$d_f = 0.27$ mm
Warp	$L_{p1} = 0.56$ mm	–	$\theta_p = 40°$	$d_p = 0.25$ mm
Twill				
Weft	$L_{f1} = 0.618$ mm	$L_{f2} = 0.487$ mm	$\theta_f = 40°$	$d_f = 0.27$ mm
Warp	$L_{p1} = 0.56$ mm	$L_{p2} = 0.41$ mm	$\theta_p = 40°$	$d_p = 0.25$ mm

Table 4 Elastic properties of weft and warp yarns

	Set of input material data		
Weft	$E_{sf} = 1889\,\mathrm{MPa}$	$G_{sf} = 756\,\mathrm{MPa}$	$\nu_f = 0.25$
Warp	$E_{sp} = 13{,}853\,\mathrm{MPa}$	$G_{sp} = 5541\,\mathrm{MPa}$	$\nu_p = 0.25$

Table 5 Mechanical properties of weft, warp and contact beams

Beam rigidity	Beams at		
	Weft	Warp	Contact
Tensile	$k_{lf_{1,2}} = \frac{E_{sf}A_f}{L_{f_{1,2}}}$	$k_{lp_{1,2}} = \frac{E_{sp}A_p}{L_{p_{1,2}}}$	$k_{lc_{1,2}} = \frac{E_{sc}A_c}{L_{c_{1,2}}}$.
Flexural	$k_{tf1} = \frac{12E_{sf}I_f}{(L_{f1})^3}$	$k_{tp1} = \frac{12E_{sp}I_p}{(L_{p1})^3}$	$k_{tc_{1,2}} = \frac{12E_{sc}I_c}{\left(L_{c_{1,2}}\right)^3}$.
Torsional	$k_{rf1} = \frac{G_{sf}J_f}{L_{f1}}$	$k_{rp1} = \frac{G_{sp}J_p}{L_{p1}}$	$k_{rc_{1,2}} = \frac{G_{sc}J_c}{L_{c_{1,2}}}$.

References

1. Goda I, Assidi M, Ganghoffer JF (2013) Equivalent mechanical properties of textile monolayers from discrete asymptotic homogenization. J Mech Phys Solids 61(12):2537–2565
2. Mourad A (2003) Description topologique de l'architecture fibreuse et modelisation mecanique du myocarde. PhD Thesis, I.N.P.L. Grenoble
3. Caillerie D, Mourad Raoult A (2006) Discrete homogenization in graphene sheet modeling. J Elasticity 84:33–68
4. Raoult A, Caillerie D, Mourad A (2008) Elastic lattices: equilibrium, invariant laws and homogenization. Ann Univ Ferrara 54:297–318
5. Dos Reis F, Ganghoffer JF (2012) Construction of micropolar continua from the asymptotic homogenization of beam lattices. Comput Struct 112–113:354–363
6. Gibson LJ, Ashby MF (1982) The mechanics of 3-dimensional cellular materials. Proc R Soc Lond Ser A 382(1782):43
7. Gibson LJ, Ashby MF, Schajer GS, Robertson CI (1982) The mechanics of two-dimensional cellular materials. Proc R Soc Lond Ser A 382(1782):25–42
8. Zhu HX, Knott JF, Mills NJ (1997) Analysis of the elastic properties of open-cell foams with tetrakaidecahedral cells. J Mech Phys Solids 45(3):319
9. Wang AJ, McDowell DL (2004) In plane stiffness and yield strength of periodic metal honeycombs. J Eng Mater Technol Trans ASME 126(2):137–156
10. Hutchinson R, Fleck N (2006) The structural performance of the periodic truss. J Mech Phys Solids 54:756–782
11. Pindera M-J, Khatam H, Drago AS, Bansal Y (2009) Micromechanics of spatially uniform heterogeneous media: a critical review and emerging approaches. Compos Struct 40:349–378
12. Charalambakis N (2010) Homogenization techniques and micromechanics: a survey and perspectives. Appl Mech Rev 63(3):1–10
13. Warren WE, Kraynik AM, Stone CM (1989) A constitutive model for two-dimensional nonlinear elastic foams. J Mech Phys Solids Struct 37:717–733
14. Warren WE, Kraynik AM (1991) The nonlinear elastic behaviour of open-cell foams. Trans ASME 58:375–381
15. Wang Y, Cuitino AM (2000) Three-dimensional nonlinear open cell foams with large deformations. J Mech Phys Solids 48:961–988
16. Hohe J, Becker W (2003) Effective mechanical behavior of hyperelastic honeycombs and two dimensional model foams at finite strain. Int J Mech Sci 45:891–913
17. Janus-Michalska M, Pęcherski RP (2003) Macroscopic properties of open-cell foams based on micromechanical modeling. Technische Mechanik, Band 23. Heft 2–4:221–231
18. Janus-Michalska J (2005) Effective models describing elastic behavior of cellular materials. Arch Metall Mater 50:595–608
19. Janus-Michalska J (2011) Hyperelastic behavior of cellular structures based on micromechanical modeling at small strain. Arch Mech 63(1):3–23
20. Vigliotti A, Deshpande VS, Pasini D (2014) Non linear constitutive models for lattice materials. J Mech Phys Solids 64:44–60
21. Sanchez-Palencia E (1980) Non-inhomogeneous media and vibration theory. Lecture notes in physics, vol 127. Springer, Berlin
22. Bakhvalov NS, Panasenko GP (1989) Homogenization averaging processes in periodic media. Kluwer, Dordrecht
23. Warren WE, Byskov E (2002) Three-fold symmetry restrictions on two-dimensional micropolar materials. Eur J Mech A 21:779–792
24. Mourad A, Caillerie DA, Raoult A (2003) A nonlinearly elastic homogenized constitutive law for the myocardium. Comput Fluid Solid Mech 2:1779–1781
25. Sab K, Pradel F (2009) Homogenisation of periodic Cosserat media. Int J Comput Appl Technol 34:60–71
26. Trovalusci P, Masiani R (1999) Material symmetries of micropolar continua equivalent to lattices. Int J Solids Struct 36:2091–108
27. Feyel F, Chaboche J-L (2000) FE2 multiscale approach for modelling the elastoviscoplastic behaviour of long fibre SiC/Ti composite materials. Comput Methods Appl Mech Eng 183(3):309–330
28. Goda I, Rahouadj R, Ganghoffer JF (2013) Size dependent static and dynamic behavior of trabecular bone based on micromechanical models of the trabecular architecture. Int J Eng Sci 72:53–77
29. Goda I, Assidi M, Ganghoffer JF (2014) A 3D elastic micropolar model of vertebral trabecular bone from lattice homogenization of the bone microstructure. Biomech Model Mechanobiol 13:53–83
30. Pietraszkiewicz W, Eremeyev VA (2009) On natural strain measures of the non-linear micropolar continuum. Int J Solids Struct 46(3):774–787
31. Holzapfel GA, Gasser TC, Ogden RW (2000) A new constitutive framework for arterial wall mechanics and a comparative study of material models. J Elasticity 61:1–48
32. Steinmann P (1994) A micropolar theory of finite deformation and finite rotation multiplicative elastoplasticity. Int J Solids Struct 31(8):1063–1084
33. Tan P, Tong L, Steven GP (1997) Modeling for predicting the mechanical properties of textile composites—a review. Composite A 28(11):903–922
34. Crookston JJ, Long AC, Jones IA (2005) A summary review of mechanical properties prediction methods for textile reinforced polymer composites. Proc. IMechE, Part L. J Mater 219:91–109
35. Peng X, Cao J (2002) A dual homogenization and finite element approach for material characterization of textile composites. Composites B 33:45–56